

Irradiation-driven escape of primordial planetary atmospheres III. Revised planetary parameters and mass-loss rates for nearby gaseous planets after Gaia DR2

Riccardo Spinelli^{1,2}, Elena Gallo³, Francesco Haardt^{1,2,4}, Andrea Caldiroli⁵, Federico Biassoni^{1,2}, and Francesco Borsa²

¹ Dipartimento di Scienza e Alta Tecnologia, Università degli Studi dell'Insubria, via Valleggio 11, I-22100 Como, Italy

² INAF – Osservatorio Astronomico di Brera, Via E. Bianchi 46, 23807 Merate, Italy

³ Department of Astronomy, University of Michigan, 1085 S University, Ann Arbor, Michigan 48109, USA

⁴ INFN, Sezione Milano-Bicocca, P.zza della Scienza 3, I-20126 Milano, Italy

⁵ Fakultät für Mathematik, Universität Wien, Oskar-Morgenstern-Platz 1, A-1090 Wien, Austria

August 4, 2022

ABSTRACT

In this paper we leverage Gaia parallactic distances to deliver revised estimates of planetary parameters and extreme ultraviolet (EUV) fluxes for a distance-limited ($\lesssim 100$ pc) sample of 27 gaseous planets – from super-Earths to hot Jupiters – with publicly available X-ray observations. Notably, the revised mass and radius imply a Saturn-like density (0.86 ± 0.09 g cm⁻³) for HD 149026 b – consistent with the lowest values reported in the literature – thus removing the need for a high metal fraction. For 20 planets with X-ray detected host stars we also derive updated atmospheric mass outflow rates making use of the 1D photoionization hydrodynamics code ATES. We note, however, how X-ray variability combined with large uncertainties in the conversion between X-rays and EUV fluxes severely affects the inferred instantaneous mass loss rates, and thus the ability to constrain/predict the integrated mass loss over a planet's lifetime.

Key words. Planets and satellites: atmospheres – X-rays: stars – Planets and satellites: physical evolution – Methods: data analysis

1. Introduction

The ongoing surge in the number of known exoplanets, including a large population of transiting systems, makes it possible for the first time to address unanswered questions of planetary physics, including their demographics and radius distribution. One such key open question concerns the impact of X-ray and extreme UV (combined, XUV) stellar radiation on the atmospheres of close-in planets, i.e., planets orbiting their star(s) at distances closer than about 0.1 A.U. It is expected that extreme XUV irradiation can heat and inflate planetary atmospheres and potentially lead to the removal of a substantial portion of the atmosphere's initial light element gas envelope (e.g. Owen & Wu 2013; Owen & Lai 2018; Wu 2019; Owen 2019). Assuming that the incident stellar XUV radiation is primarily converted into expansion work, the current rate of mass loss \dot{M} from an irradiated atmosphere can be expected to depend directly upon the incident XUV flux and inversely upon the planetary density (Watson et al. 1981; Erkaev et al. 2007). In practice, numerical work has shown that the validity of this “energy-limited” approximation is fairly limited, and that efficiency of this process varies greatly amongst different systems (e.g. Lammer et al. 2003; Yelle 2004; Tian et al. 2005; Muñoz 2007; Murray-Clay et al. 2009; Owen & Jackson 2012; Erkaev et al. 2013; Erkaev et al. 2016; Salz et al. 2016; Salz et al. 2016). In Paper II of this series (Caldirolì et al. 2022), we make use of the open-source, 1D photo-ionization code ATES (Caldirolì et al. 2021; Paper I of this series) to provide a physically-motivated, quantitative as-

essment of the evaporation efficiency as a function of both stellar irradiation and planetary gravity.

An accurate estimate of the XUV irradiation (here defined as the flux at the planetary surface) hinges on accurate measurements of stellar distance as well as orbital distance; the latter is often derived from stellar parameters, typically using stellar models or empirically-calibrated stellar relations. As noted by Stassun et al. (2017), the use of stellar models may be precise but not always accurate, owing to the uncertainties in stellar evolution models, including the role of stellar rotation and its relationship with age and activity. The second Gaia data release (Gaia Collaboration et al. 2018; Riello et al. 2018; Sartoretti et al. 2018; Luri et al. 2018; hereafter GDR2) provides parallactic distance determinations for over a billion stars. These enable more reliable estimates of stellar XUV luminosities as well as planetary parameters, and thus atmospheric mass loss rates.

In this Paper, the third of the series, we present new and/or revised parameters for a distance-limited sample of 27 planet-hosting systems with available X-ray observations, totaling 27 planets. Specifically, we (i) perform a homogeneous X-ray spectra analysis, and provide revised X-ray luminosities–based on GDR2 distances; (ii) obtain updated planetary parameters, including density and XUV irradiation; (iii) run ATES for all the (22) X-ray detected systems, and derive stable solutions for the instantaneous atmospheric mass loss rates for 20 planets.

Our work is organized as follows. In § 2 we present the sample; § 3 describes the X-ray observations analysis and results; § 4 presents the method for estimating new planetary parameters based on the GDR2 distances; § 5 makes use of the above to de-

rive (whenever possible) new mass outflow rates. We discuss our results in § 6.

2. Sample

We draw our targets from the `exoplanet.eu`¹ database, selecting planetary systems with (i) both transit and radial velocity data; (ii) (pre-Gaia DR2) distances within ~ 100 pc; (iii) average orbital distances within 0.1 A.U., to select for highly irradiated systems; (iv) planetary radii in excess of $1.5 R_{\oplus}$ (or $0.134 R_J$), above which a primordial (H/He-rich) atmosphere may be retained (Lopez & Fortney 2014). Out of these, we sub-select for host stars with publicly available X-ray spectroscopic data, either with XMM-Newton or the Chandra X-ray Observatory, yielding a final sample of 26 planetary systems comprising 27 planets. A complete list of planetary parameters for the target sample can be found in Table 1.

Below, we provide a brief description of each system, with an emphasis on recent constraints or predictions concerning atmospheric escape and its detectability. Below, we follow Koppa-[rapu et al. \(2018\)](#), who divide planets into rocky ($0.5 - 1.0 R_{\oplus}$), super-Earths ($1.0 - 1.75 R_{\oplus}$), sub-Neptunes ($1.75 - 3.5 R_{\oplus}$), sub-Jovians ($3.5 - 6.0 R_{\oplus}$) and Jovians ($6 - 14.3 R_{\oplus}$) based on their planet sizes, and “hot”, “warm” and “cold” based on the incident stellar flux where different chemical species are condensing in the atmosphere (see table 3 in [Koppa-\[rapu et al. 2018\]\(#\)](#) for details).

- together with WASP-80b ([Triaud et al. 2013](#)) and WASP-10 ([Christian et al. 2009](#)), WASP-43b ([Hellier et al. 2011](#)) represents one of the rare instances of a transiting hot Jupiter around a late K/early-M star. This makes them promising targets for detecting and probing atmospheric escape ([Oklopčić 2019](#)), albeit the recent non-detection of metastable helium in the transit spectrum of WASP-80b poses considerable theoretical challenges ([Fossati et al. 2022](#)).
- HD 97658b ([Howard et al. 2011](#)) is a moderately irradiated super-Earth whose low density (3.9 g cm^{-3} , [Van Grootel et al. 2014](#)) is compatible with a massive steam envelope that could be dissociated by stellar irradiation at high altitudes. Nevertheless, the non-detection of neither Lyman- α nor helium during transit suggests that the system may lack an extended, evaporating hydrogen atmosphere ([Bourrier et al. 2017](#); [Kasper et al. 2020](#)).
- WASP-69b ([Anderson et al. 2014](#)) is a hot Jupiter orbiting an active K-type star. [Nortmann et al. \(2018\)](#) reports on the detection of excess helium absorption during transit; the complex line shape during and post transit is consistent with an out-flowing cometary atmosphere.
- HD 149026b ([Sato et al. 2005](#)) is a Jovian planet with mass close to Saturn’s, orbiting a G star. Several studies ([Sato et al. 2005](#); [Charbonneau et al. 2006](#); [Winn et al. 2008](#); [Nutzman et al. 2009](#)) conclude that the planet is significantly denser than Saturn, seemingly implying a metal-rich composition. The presence of metals in its atmosphere has also been proposed to explain the inferred high density of HAT-P-20 b ([Deming et al. 2015](#)) compared to other systems with similar masses ([Bakos et al. 2011](#)).
- HD 189733b ([Bouchy et al. 2005](#)) and HD 209458b ([Charbonneau et al. 2000](#); [Henry et al. 2000](#)) are among the closest (and hence best studied) transiting hot Jovian planets. The detection of Lyman- α absorption in transit in these systems provided the first observational evidence for an escaping atmosphere ([Vidal-Madjar et al. 2003](#); [Lecavelier des Etangs et al. 2010](#)). [Salz et al. \(2018\)](#) and [Alonso-Floriano et al. \(2019\)](#) have also reported the detection of metastable helium absorption in the upper atmosphere of HD 189733b and HD 209458b. To explain the different helium absorption depths measured in different transits, [Zhang et al. \(2022\)](#) proposed stellar XUV variability.
- WASP-77Ab ([Maxted et al. 2013](#)) is a transiting hot Jovian orbiting around a moderately bright G-type star (the member of a visual binary). WASP-18b ([Hellier et al. 2009](#)) is an extremely close-in hot Jupiter, with $10 M_J$ and an orbital period of 0.94 days. In spite of the extreme orbital parameters, this system is remarkably inactive ([Miller et al. 2012](#)). Similarly, the large mass ($8 M_J$) and relatively short orbital period (~ 5.63 d) of HAT-P-20 b ([Bakos et al. 2007](#)) make it a promising target for planet-star interactions studies.
- GJ 436b ([Butler et al. 2004](#)), GJ 3470b ([Bonfils et al. 2012](#)), HAT-P-11b ([Bakos et al. 2010](#)) and K2-25b ([Mann et al. 2016](#)) are the four closest, transiting sub-Jovians planets. As noted by [King et al. \(2018\)](#) only one other transiting planet within 100 pc (HD 3167c) has a radius between 3 and $5 R_{\oplus}$. GJ 436b is the most illustrative example for the presence of a planetary tail of material, inferred through Lyman- α observations ([Kulow et al. 2014](#); [Ehrenreich et al. 2015](#); [Lavie et al. 2017](#)). [Nortmann et al. \(2018\)](#) provided only an upper limit for helium signals in the atmospheres of GJ 436b. Lyman- α absorption during GJ 3470 b transits is observed by [Bourrier et al. \(2018\)](#), while [Mansfield et al. \(2018\)](#) report the detection of helium in the atmosphere of HAT-P-11 b. K2-25b orbits a relatively young (~ 727 Myr) M4.5 host with a period of 3.48 days. The planet is similar to GJ 436b, although [Rockcliffe et al. \(2021\)](#) report on a Lyman-alpha non-detection during transit. In addition, the combination of the inferred high-density and young age for this system challenges prevailing theories of planet formation ([Stefansson et al. 2020](#)).
- WASP 107b ([Anderson et al. 2017](#)) is an extremely low density Jovian planet (0.13 g cm^{-3} , [Piaulet et al. 2021](#)) and associated with the first detection of metastable helium during transit ([Spake et al. 2018](#)). 55 Cnc e ([McArthur et al. 2004](#)) is an ultra-short period planet ($P < 1$ day) whose radius sits right at the upper limit of the so-called small planet “radius gap” ([Fulton et al. 2017](#)), i.e., between 1.5 and $2 R_{\oplus}$. The absence of helium and Lyman- α absorption during transit ([Ehrenreich et al. 2012](#); [Zhang et al. 2021](#)) suggests that the planet has probably already lost its envelope.
- GJ 9827b,c,d ([Rodriguez et al. 2018](#)) are three super-Earths orbiting a bright K6 star with planetary radii that span across the radius gap. In particular, GJ 9827b’s radius falls between that of super-Earths and sub-Neptunes ([Fulton et al. 2017](#)). [Carleo et al. \(2021\)](#) and [Kasper et al. \(2020\)](#) reported a non-detection of helium absorption for GJ 9827 b and GJ 9827 d.
- Au Mic b ([Plavchan et al. 2020](#)) is a sub-Jovian planet just above the radius gap, orbiting a young (22 Myr) fastly rotating (~ 4.85 d) pre-main sequence M dwarf. It represents a rare target for studying atmospheric loss during early evolutionary stages, when the host star is likely very active and has a much higher XUV bolometric ratio than after the first 100 Myr (e.g., [Vilhu 1984](#); [Vilhu & Walter 1987](#); [Wright et al. 2011](#)).
- GJ 1214b ([Charbonneau et al. 2009](#)) is a super-Earth orbiting an M-dwarf; it is best known for the claim that high-

¹ <http://exoplanet.eu/>

Table 1. Planet sample; GDR2 distance (1); host star effective temperature (2); host star spectral type (3); host star radius (4); ratio between the orbital semi-major axis and the stellar radius (corrected for eccentricity unless otherwise noted) (5); orbital period (6), optical transit depth (7); radial velocity semi-amplitude (8); orbital inclination angle (9); eccentricity (10); periastron argument (11); * indicates not corrected for eccentricity.

	d	T_{eff}	Spectral	R_*	$(a/R_*)_E$	P	ΔF	K	i	e	ω	Ref.
	[pc]	[K]	type	[R_\odot]		[d]	[%]	[m/s]				
	(1)	(2)	(3)	(4)	(5)	(6)	(7)	(8)	(9)	(10)	(11)	
Host FGK												
HAT-P-2 b (S16)	127.77	6338	F8	1.73	8.99	5.633	0.522	983.9	86.72	0.517	185	1
WASP-18 b (S16)	123.48	6462	F6	1.24	3.48	0.941	1.04	1814	83.5	0.005	-85	2
HAT-P-20 b (S16)	71.03	4501	K7	0.73	11.36	2.875	2.40	1249.5	86.88	0.017	343	3
WASP-10 b (S16)	141.00	4878	K5V	0.67	11.90*	3.093	2.48	543.0	88.81	0.06	152	4,5
WASP-38 b (S16)	136.24	6170	F8	1.47	12.15	6.872	0.71	253.8	88.83	0.032	-19	6
WASP 8 b (S16)	89.96	5610	G6	0.99	18.20	8.159	1.276	221.1	88.55	0.304	274	7
WASP-43 b (S16)	86.75	4306	K7V	0.66	4.97	0.814	2.52	551.0	82.11	0	90	3
WASP-77 A b (S16)	105.17	5556	G8V	0.95	5.33	1.360	1.78	323.4	88.91	0.007	-166	2
HD 189733 b (S16)	19.76	5015	K2V	0.78	8.99	2.219	2.47	200.56	85.71	0	90	8,9
WASP-80 b (S16)	49.79	4076	K7V	0.61	12.63	3.068	2.94	109.0	89.02	0.002	94	10
HD 209458 b (S16)	48.30	6076	F9V	1.18	8.78*	3.525	1.49	84.9	86.71	0.01	0.0	8,11
HD 149026 b (S16)	75.86	6076	G0 IV	1.47	5.98*	2.876	0.27	37.9	84.50	0.003	100	12,13
WASP-29 b	87.60	4732	K4V	0.81	12.50	3.923	0.933	36.0	89.47	<0.059	-	5,14
WASP 69 b	49.96	4875	K5	0.82	12.00	3.868	1.79	38.1	86.71	0	90	15,16
HAT-P-11 b (S16)	37.77	4757	K4	0.77	14.64	4.888	0.343	11.6	88.99	0.265	-162	17,18
55 Cnc e (S16)	12.59	5306	K0IV-V	0.95	3.52	0.737	0.033	6.02	83.59	0.05	86	7
HD 97658 b (S16)	21.56	5192	K1V	0.75	24.2*	9.490	0.07	2.90	89.45	0.063	-9	19,20
WASP-107 b	64.74	4233	K6	0.73	18.16*	5.721	2.08	14.1	89.8	0.06	40	21,22
HD 219134 b	6.53	4787	K3V	0.80	10.48	3.092	0.0326	2.381	85.01	0	0	23
GJ 9827 d	29.66	4174	K6V	0.65	19.7	6.202	0.096	2.50	87.39	0	0	24
GJ 9827 b	29.66	4174	K6V	0.65	6.62	1.209	0.059	2.84	85.73	0	0	24
Host M												
K2-25 b	44.96	3207	M4.5	0.32	21.09	3.485	1.155	27.9	87.16	0.43	120	25
GJ 436 b (S16)	9.75	3416	M2.5	0.43	14.54	2.644	0.68	17.59	86.86	0.162	372	26
LHS 1140 b	14.99	3016	M4.5	0.21	96.4	24.737	0.493	4.21	89.88	<0.096	90	27
AU Mic b	9.72	3992	M1V	0.61	19.1	8.463	0.246	8.50	89.5	0	-	28
GJ 3470 b (S16)	29.42	3725	M1.5	0.55	13.94	3.337	0.584	9.2	88.88	0.017	1.7	29
GJ 1214 b (S16)	14.64	3026	M4.5V	0.22	14.62	1.580	0.0139	10.9	89.19	<0.23	0	30

References. For all sources: d from [Gaia Collaboration et al. \(2018\)](#). For all the FGK stars plus Au Mic T_{eff} is from [Andrae et al. \(2018\)](#). For out of filter M dwarfs we use the results of ([Andrae et al. 2018](#)), assuming T_{eff} from [Stefansson et al. \(2020\)](#) for K2-25, [von Braun et al. \(2012\)](#) for GJ 436, [Spinelli et al. \(2019\)](#) for LHS 1140, from [Palle et al. \(2020\)](#) for GJ 3470, and [Anglada-Escudé et al. \(2013\)](#) for GJ 1214. R_* is from [Andrae et al. \(2018\)](#) for FGK stars. For M dwarfs R_* are obtained from T_{eff} using the empirical relationships derived by [Morrell & Naylor \(2019\)](#) using GR2 data. $(a/R_*)_E$, P , ΔF , K , i , e and ω are from the following references: (1) [Bakos et al. \(2010\)](#); (2) [Cortés-Zuleta et al. \(2020\)](#); (3) [Esposito et al. \(2017\)](#); (4) [Barros et al. \(2013\)](#); (5) [Bonomo et al. \(2017\)](#); (6) [Simpson et al. \(2011\)](#); (7) [Bourrier et al. \(2018\)](#); (8) [Southworth \(2010\)](#); (9) [Cegla et al. \(2016\)](#); (10) [TriAUD et al. \(2015\)](#); (11) [Rosenthal et al. \(2021\)](#); (12) [Stevenson et al. \(2012\)](#); (13) [Knutson et al. \(2014\)](#); (14) [Saha & Sengupta \(2021\)](#); (15) [Anderson et al. \(2014\)](#); (16) [Casasayas-Barris et al. \(2017\)](#); (17) [Huber et al. \(2017\)](#); (18) [Yee et al. \(2018\)](#); (19) [Ellis et al. \(2021\)](#); (20) [Dragomir et al. \(2013\)](#); (21) [Piaulet et al. \(2021\)](#); (22) [Anderson et al. \(2017\)](#); (23) [Gillon et al. \(2017\)](#); (24) [Rodríguez et al. \(2018\)](#); (25) [Stefansson et al. \(2020\)](#); (26) [Lanotte et al. \(2014\)](#); (27) [Lillo-Box et al. \(2020\)](#); (28) [Martioli et al. \(2021\)](#); (29) [Biddle et al. \(2014\)](#); (30) [Anglada-Escudé et al. \(2013\)](#)

altitude clouds would obscure the deeper atmospheric layers ([Kreidberg et al. 2014](#)). Recently, [Orell-Miquel et al. \(2022\)](#) reported a significant ($>4\sigma$) detection of metastable helium in this system during one transit observed with the CARMENES spectrograph, in contrast with previous non-detections ([Kasper et al. 2020](#); [Petit dit de la Roche et al. 2020](#)). New observations are expected to eventually confirm the presence of an extended atmosphere.

- LHS 1140b ([Dittmann et al. 2017](#)) and LHS 1140c ([Ment et al. 2019](#)) are two super-Earths orbiting an M-dwarf. LHS 1140 b is located within the so-called habitable zone, where temperature and pressure would be suitable for the presence

of liquid water on the planetary surface (e.g. [Kasting et al. 1993](#); [Kopparapu et al. 2013](#)). As such, this system represents a key target for future astrobiological studies ([Spinelli et al. 2019](#); [Wunderlich et al. 2021](#); [Edwards et al. 2021](#)).

- HD 219134 b ([Motalebi et al. 2015](#)) is the closest transiting exoplanet and the innermost of a planetary system with other four planets in tight orbit (<0.4 AU) and one distant Jovian planet (3 AU), with an architecture roughly similar to the solar system’s one ([Vogt et al. 2015](#)). [Folsom et al. \(2018\)](#) derive the stellar wind mass-loss rate of the star of the system ($10^{-14} M_\odot \text{ yr}^{-1}$, half the solar value) using HST/STIS observations of the Lyman- α line.

- WASP-8b (Queloz et al. 2010) is a hot Jupiter in an eccentric orbit that is misaligned with the stellar rotation axis, and moving in a retrograde direction. WASP-29 b (Hellier et al. 2010) is a low-density Jovian planet for which the reported Lyman- α upper limit argues against the presence of an escaping hydrogen atmosphere (dos Santos et al. 2021).

Table 2. X-ray observation log; instruments (1) (C for Chandra, X for XMM), observation ID (2), observation date (3), exposure time (4), Principal Investigator (5).

	Instr.	ObsID	Date	Exp. time	PI
	(1)	(2)	(3)	(4)	(5)
				[ks]	
Host FGK					
HAT-P-2	C	15707	2013-11-16	10	Salz
WASP-18	C	14566	2013-02-26	85	Pillitteri
HAT-P-20	C	15711	2013-11-24	10	Salz
WASP-10	C	15710	2013-11-15	10	Salz
WASP-38	C	15708	2014-01-18	10	Salz
WASP 8	C	15712	2013-10-23	10	Salz
WASP-43	X	0694550101	2012-05-11	18	Grosso
WASP-77A	C	15709	2013-11-09	10	Salz
WASP80	X	0744940101	2014-05-15(A)	19	Salz
	X	0764100801	2015-05-13 (B)	33	Wheatley
HD 209458	X	0130920101	2000-11-29(A)	19	Jansen
	X	0148200101	2003-06-11(B)	23	Bertaux
	X	0404450101	2006-11-14(C)	34	Wheatley
	C	16667	2016-06-17(D)	29	Czesla
HD 149026	X	0763460301	2015-08-14	20	Salz
WASP 29	X	0804790201	2017-05-14	8	Sanz-Forcada
WASP-69	X	0783560201	2016-10-21	31	Salz
HAT-P-11	X	0764100701	2015-05-19(A)	32	Wheatley
	C	16669	2015-11-14(B)	8	Miller
55 Cnc	X	0551020801	2009-04-11(A)	14	Schmitt
	C	14401	2012-03-07(B)	11	Wheatley
	C	14402	2012-04-05(C)	20	Wheatley
HD97658	X	0764100601	2015-06-04(A)	34	Wheatley
	C	16668	2015-10-17(B)	13	Miller
	C	18724	2015-12-11(C)	20	Wheatley
	C	18725	2016-03-05(D)	20	Wheatley
WASP 107	X	0830190901	2018-06-22	63	Shartel
HD 219134	X	0784920201	2016-06-13	38	Wheatley
GJ 9827	X	0821670101	2018-05-27(A)	22	Drake
	X	0821670201	2018-06-23(B)	17	Drake
	X	0821670301	2018-11-27(C)	11	Drake
Host M					
K2-25	X	0782061001	2017-03-07	19	Agueros
GJ 436	X	0556560101	2008-12-10(A)	33	Wheatley
	C	14459	2013-02-16(B)	19	Ehrenreich
	C	15537	2013-04-18(C)	19	Ehrenreich
	C	15536	2013-06-18(D)	20	Ehrenreich
	C	15642	2014-06-23(E)	19	Ehrenreich
	C	17322	2015-06-25(F)	9	France
	C	17321	2015-06-26(G)	20	France
	X	0764100501	2015-11-21(H)	27	Wheatley
LHS 1140	X	0822600101	2018-12-21	64	Dittmann
Au Mic	X	0111420101	2000-10-13 (A)	56	Brinkman
	X	0822740301	2018-10-10 (B)	134	Kowalski
	X	0822740401	2018-10-12 (C)	137	Kowalski
	X	0822740501	2018-10-14 (D)	139	Kowalski
	X	0822740601	2018-10-16 (E)	70	Kowalski
GJ 3470	X	0763460201	2015-04-15	18	Salz
GJ 1214	X	0724380101	2013-09-27(A)	36	Sairam
	C	15725	2014-06-07(B)	31	Brown

3. X-ray luminosities

The targets were selected for having publicly available X-ray observations with either XMM-Newton or Chandra (or both). Table 2 and Table 3 (the latter is specific to HD 189733, which was targeted 31 times) list the full observations' log.

XMM-EPIC-pn (European Photon Imaging Camera) data were analyzed using the Scientific Analysis System (SAS 15.0.0), while Chandra ACIS-S (Advanced CCD Imaging Spectrometer) and HRC (High Resolution Camera) observations were reduced with the Chandra Interactive Analysis of Observations software package (CIAO 4.13). For each observation, we estimated the source sky position using J2000 coordinates and proper motion provided by SIMBAD². An X-ray source was detected within 1.0 arcsec of the target star optical position (after accounting for proper motion) with a significance greater than 3σ (Li & Ma 1983) in at least 1 observation for 22 out of 26 target stars.

Photometry was performed within a radius of ~ 15 and ~ 2 arcsec for EPIC and ACIS/HRC, respectively, and centered on the nominal optical position of the target star, corrected for proper motion. For the XMM observations of HD 189733 and LHS 1140 we adopted a 10 arcsec extraction radius, to avoid contamination from nearby sources (Pillitteri et al. 2010; Spinelli et al. 2019). The background was extracted from a contamination-free circular region with a radius of about 30 arcsec for all targets.

We analysed the background-corrected spectra with XSPEC 12.11.1 (Arnaud 1996). Owing to the low numbers of counts (the median of the net counts of the sources is 106 counts), each spectrum was binned to have at least one count per energy bin. The resulting spectra were fitted using C-statistics (hereafter cstat; Cash 1979), and assuming a thermal plasma emission model. Metal abundances were fixed to the solar value as derived by Asplund et al. (2009) (in no case did leaving the abundance free to vary improve the fit).

We modeled the X-ray flux attenuation arising from interstellar absorption using the TBABS model (Wilms et al. 2000). For each system, the hydrogen column density was set equal to the product between the distance and a mean interstellar hydrogen density of 0.1 cm^{-3} , in agreement with LIC model (Linsky et al. 2000; Redfield & Linsky 2008³).

In order to assess whether a one, two or three temperature APEC model provides a better description of the data, we proceeded with a parametric bootstrap procedure, as follows. For each target star, we picked a model (e.g., single temperature APEC) and fit the data; we then used the best-fitting model to simulate 1,000 spectra with the XSPEC tool *fakelit*. If the cstat of the best-fit model to the actual data fell within the cstat distribution of the simulated data models, we considered the model as acceptable. Conversely, a model was rejected if its cstat was greater than 95% of the cstats of the simulated spectral models. In those cases where both models were acceptable, we chose

² <http://simbad.u-strasbg.fr/simbad/>

³ <http://lism.wesleyan.edu/ColoradoLIC.html>

Table 3. Observation log for HD 189733 (S16); instruments (1) (C for Chandra, X for XMM), observation ID (2), date (3), exposure time (4), Principal Investigator (5).

ObsID	Instr.	Date	Exp. time	PI
		[ks]		
(1)	(2)	(2)	(3)	(4)
X	050607201	2007-04-18(A)	55	Wheatley
X	0600970201	2009-05-18(B)	37	Wolk
X	0672390201	2011-04-30(C)	39	Pillitteri
C	12340	2011-07-05(D)	19	Poppenhaeger
C	12343	2011-07-12(E)	20	Poppenhaeger
C	12344	2011-07-16(F)	18	Poppenhaeger
C	12345	2011-07-18(G)	20	Poppenhaeger
C	12341	2011-07-21(H)	20	Poppenhaeger
C	12342	2011-07-23(I)	20	Poppenhaeger
X	0690890201	2012-05-07(J)	62	Pillitteri
X	0692290201	2013-05-09(K)	39	Wheatley
X	0692290301	2013-11-03(L)	37	Wheatley
X	0692290401	2013-11-21(M)	42	Wheatley
X	0744980201	2014-04-05(N)	48	Wheatley
X	0744980301	2014-05-02(O)	34	Wheatley
X	0744980401	2014-05-13(P)	40	Wheatley
X	0744980501	2014-05-15(Q)	32	Wheatley
X	0744980601	2014-05-17(R)	32	Wheatley
X	0744980801	2014-10-17(S)	37	Wheatley
X	0744980901	2014-10-19(T)	34	Wheatley
X	0744981001	2014-10-22(U)	40	Wheatley
X	0744981101	2014-10-24(V)	39	Wheatley
X	0744981301	2014-11-08(W)	35	Wheatley
X	0744981201	2014-11-11(X)	44	Wheatley
X	07449814901	2014-11-13(Y)	32	Wheatley
X	0744980701	2014-11-15(Z)	39	Wheatley
X	0748391401	2015-04-03(AA)	47	Schartel
X	0744981501	2015-04-13(AB)	45	Wheatley
X	0744981601	2015-04-17(AC)	41	Wheatley
X	0744981701	2015-04-19(AD)	38	Wheatley
X	0748391501	2015-04-23(AE)	44	Schartel

the best-fit model according to the Akaike information criterion (Akaike 1974). In our analysis we compute the AIC value for both three model as $AIC = 2K + C$, where C is the cstat and K the number of free parameter in the model. If a difference between two AIC is larger than 4 we chose the model with the lowest AIC, otherwise we chose the model with the lowest number of temperatures. All of the X-ray spectra, binned to lower resolution for better visualization, are shown in Figures 1 and 2 along with their best-fit models.

For marginally significant detections (less than 3σ , i.e., HD97658-D, WASP-10, HD209458-A/B/C, WASP-38, WASP-18, WASP-29, 55Cnc-B), we estimated the 3σ confidence upper limits following Gehrels (1986). Count rate limits were converted to flux limits using PIMMS⁴ v.4.11a.

The resulting fluxes and/or upper limits (in the energy bands 0.2–2.4 keV for XMM observations and 0.243–2.4 keV for Chandra) are listed in Table 4.

In the following, we discuss our revised X-ray luminosities vis a vis previous values reported in the literature, when available. For the purpose of a systematic comparison with these mass loss rates, whenever possible we refer to the work by Salz et al. (2016) (hereafter S16), and references therein, who assembled X-ray measurements/estimates for most of our targets, i.e.: HAT-P-2, WASP-18, HAT-P-20, WASP-10, WASP-38, WASP-8, WASP-43, WASP-77 A, HD 189733, WASP-80, HD 209458, HD 149026, HAT-P-11, 55 Cnc, HD 97658, GJ 436, GJ 3470, GJ 1214. In addition, our sample includes WASP-29, WASP-107, HD 219134, GJ 9827, K2-25, LHS 1140, AU Mic; when available, we compare our results for these systems, too, with the literature.

3.1. HAT-P-2 (S16)

Our analysis of the Chandra observation available for this system yields a flux of $5.50^{+0.74}_{-0.79} \times 10^{-14} \text{ erg cm}^{-2} \text{ s}^{-1}$, in agreement with the value obtained by Salz et al. (2015) and reported by S16. The revised GDR2 distance ($127.77 \pm 0.42 \text{ pc}$ vs. $114 \pm 10 \text{ pc}$) implies a luminosity of $1.07 \pm 0.15 \times 10^{29} \text{ erg s}^{-1}$.

3.2. WASP-18 (S16)

WASP-18 is not significantly detected in the Chandra X-ray observation available for this system. We estimate a 3σ upper limit of $0.10 \times 10^{-14} \text{ erg cm}^{-2} \text{ s}^{-1}$, higher than that found by Salz et al. (2015) and reported by S16 ($0.06 \times 10^{-14} \text{ erg cm}^{-2} \text{ s}^{-1}$). The revised GDR2 distance ($123.48 \pm 0.37 \text{ pc}$ vs. $99 \pm 10 \text{ pc}$) implies a higher yet X-ray luminosity upper limit, of $1.82 \times 10^{27} \text{ erg s}^{-1}$ (vs. $7 \times 10^{26} \text{ erg s}^{-1}$ in S16).

3.3. HAT-P-20 (S16)

Based on our analysis of the Chandra observation available for this system we measure a flux of $1.78^{+0.28}_{-0.35} \times 10^{-14} \text{ erg cm}^{-2} \text{ s}^{-1}$, in excellent agreement with the value reported by Salz et al. (2015) and used by S16. At a distance of 71.03 pc (GDR2) this measurement implies an X-ray luminosity of $1.07^{+0.17}_{-0.21} \times 10^{28} \text{ erg s}^{-1}$.

3.4. WASP-10 (S16)

Based on our analysis of the Chandra observation available for this system, the target is only marginally detected, at the 1.7σ confidence level. Assuming an APEC model with temperature 0.3 keV, we derive a 3σ upper limit of $< 0.90 \times 10^{-14} \text{ erg cm}^{-2} \text{ s}^{-1}$, slightly more stringent than the value of $1.3^{+0.01}_{-1.3} \times 10^{-14} \text{ erg cm}^{-2} \text{ s}^{-1}$ reported by S16. Adopting the new GDR2 distance ($141.00 \pm 0.75 \text{ pc}$ vs. $90 \pm 20 \text{ pc}$), the X-ray luminosity (limit) for this system increases by a factor of 2.5, to $\lesssim 2.14 \times 10^{28} \text{ erg s}^{-1}$.

3.5. WASP-38 (S16)

For this system, the Chandra data yield a 3σ limit of $0.56 \times 10^{-14} \text{ erg cm}^{-2} \text{ s}^{-1}$ (vs. $0.8 \times 10^{-14} \text{ erg cm}^{-2} \text{ s}^{-1}$ given by S16). Considering the new GDR2 distance ($136.24 \pm 0.80 \text{ pc}$

⁴ <https://cxc.harvard.edu/toolkit/pimms.jsp>

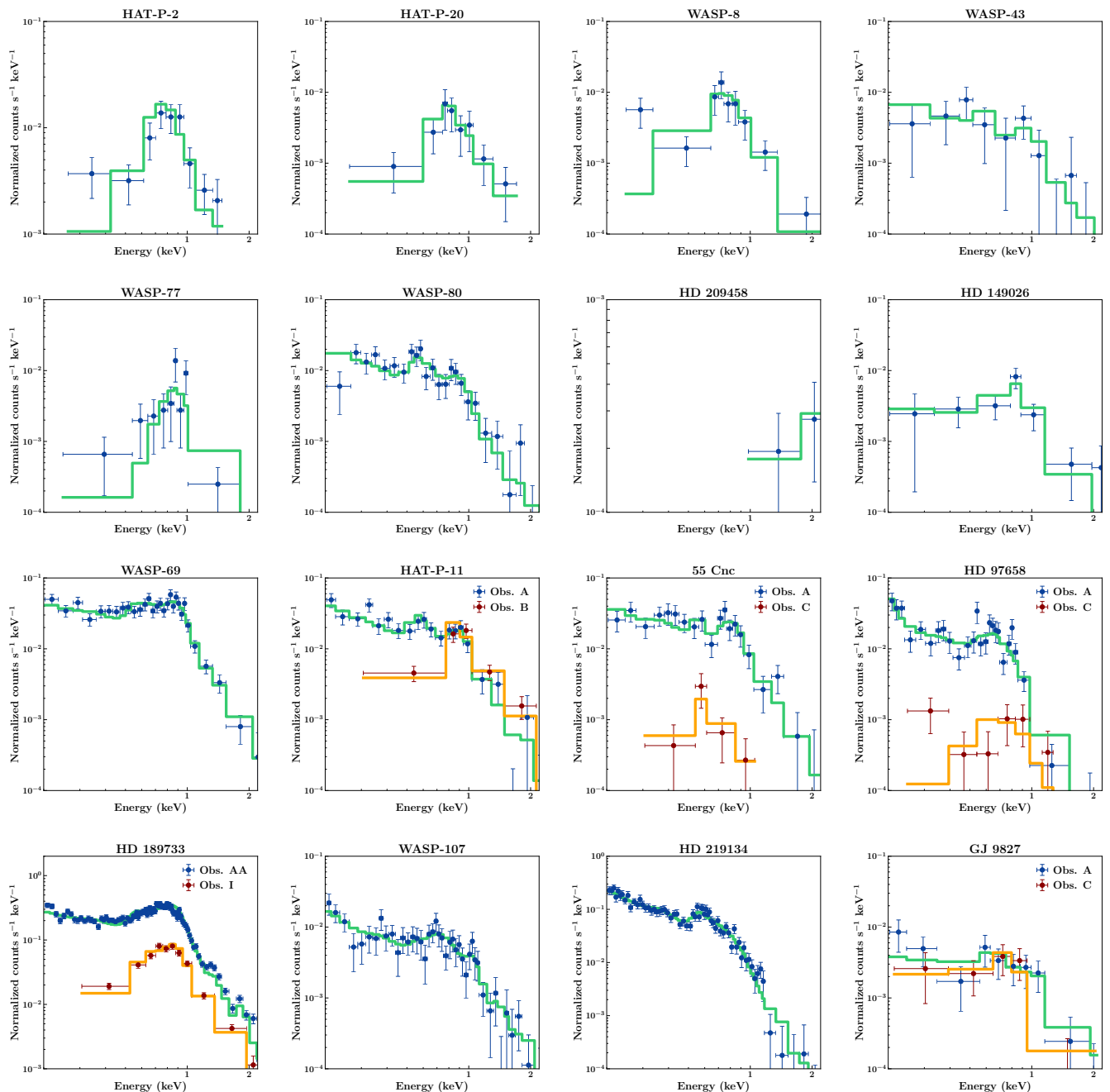


Fig. 1. EPIC-pn and ACIS-S (binned) X-ray spectra for the X-ray detected FKG-type host stars. Count rates are shown in blue/red with error bars; the green/orange histograms represent the best-fit (one, two, or three temperature) APEC model. For targets with multiple epochs and significant variability we show the highest and the lower flux cases.

vs. 110 ± 20 pc) the resulting X-ray luminosity (limit) is $\lesssim 1.24 \times 10^{28}$ erg s $^{-1}$.

3.6. WASP-8 (S16)

Based on our analysis of the Chandra observation available for this system, we measure a flux of $3.50^{+0.61}_{-0.71} \times 10^{-14}$ erg cm $^{-2}$ s $^{-1}$, consistent within the errors with the value reported by S16. At a distance of 89.69 pc (GAIA DR2) this measurement implies an X-ray luminosity of $3.37^{+0.32}_{-1.01} \times 10^{28}$ erg s $^{-1}$.

3.7. WASP-43 (S16)

Based on our analysis of the XMM observation available for this system we measure a flux of $0.75^{+0.12}_{-0.20} \times 10^{-14}$ erg cm $^{-2}$ s $^{-1}$, consistent within the errors with the value listed by S16, and derived by Czesla et al. (2013). Adopting the new GDR2 distance (86.75 ± 0.33 pc vs 80 ± 30 pc) this measurement implies an X-ray luminosity of $6.75^{+1.09}_{-1.80} \times 10^{27}$ erg s $^{-1}$, still consistent within the errors with the value reported by S16.

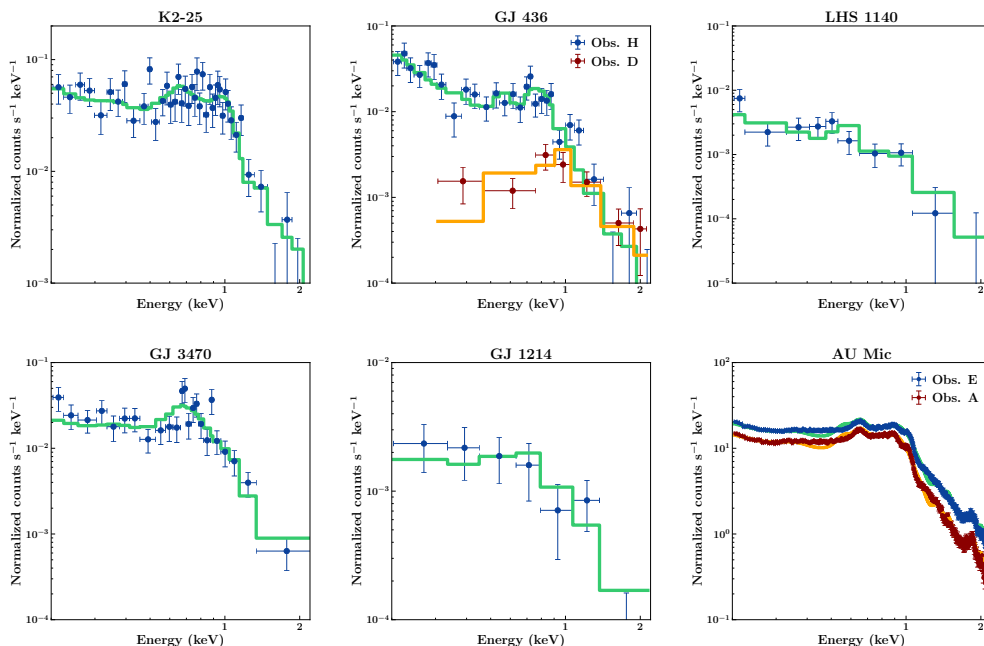


Fig. 2. Same as Figure 1, but for M-type hosts.

3.8. WASP-77 A (S16)

Based on our analysis of the Chandra observation available for this system, we measure a flux of $1.24^{+0.16}_{-0.35} \times 10^{-14}$ erg cm $^{-2}$ s $^{-1}$ in excellent agreement with the value listed S16, and derived by Salz et al. (2015). Adopting the new GDR2 distance (105.17 ± 1.20 pc vs 93 ± 5 pc) this measurement implies an X-ray luminosity of $1.64^{+0.21}_{-0.46} \times 10^{28}$ erg s $^{-1}$, consistent within the errors with the value reported by S16.

3.9. WASP-80 (S16)

This system was observed twice with XMM; we measure a flux of $[1.77^{+0.16}_{-0.28} - 1.70^{+0.11}_{-0.19}] \times 10^{-14}$ erg cm $^{-2}$ s $^{-1}$ for observations A and B respectively, consistent within the errors with the value quoted by S16, and based again on Salz et al. (2015), as well as King et al. (2018) (K18 hereafter). The revised GDR2 distance (49.78 ± 0.12 pc vs. 60 ± 20 pc) implies a luminosity between $[5.26^{+0.47}_{-0.84} - 5.05^{+0.32}_{-0.57}] \times 10^{27}$ erg s $^{-1}$.

3.10. HD 209458 (S16)

This system was observed four times, three with XMM (although observation B was affected by a filter-wheel failure) and once with Chandra, but only detected in the Chandra data (observation D). For that, we measure a flux of $2.25^{+1.12}_{-2.25} \times 10^{-14}$ erg cm $^{-2}$ s $^{-1}$, where the large uncertainties are due to the degeneracy between the emission measure and the temperature in the model. The most stringent 3σ upper limit measured by XMM (observation C) corresponds to a flux $\lesssim 0.26 \times 10^{-14}$ erg cm $^{-2}$ s $^{-1}$, indicating statistically significant X-ray variability. This value is less stringent than the value obtained by Sanz-Forcada et al. (2011) (and reported by S16) with the same data ($\lesssim 0.10 \times 10^{-14}$ erg cm $^{-2}$ s $^{-1}$). At a distance of 48.30 pc (GDR2), these measurements imply an X-ray luminosity range between $\lesssim 7.26 \times 10^{26}$ erg s $^{-1}$ and $6.28^{+3.13}_{-6.28} \times 10^{27}$ erg s $^{-1}$.

3.11. HD 149026 (S16)

Based on the archival XMM observation we measure a flux of $0.75^{+0.04}_{-0.21} \times 10^{-14}$ erg cm $^{-2}$ s $^{-1}$, in agreement with the value reported by K18 based on the same data. S16 reported a significantly higher flux (5.33×10^{-14} erg cm $^{-2}$ s $^{-1}$) on the basis of the empirical relation with stellar mass and rotation rate derived by Pizzolato et al. (2003) for a sample of main sequence stars. As suggested by K18, the discrepancy is likely due to the sub-giant nature of HD 149026. At a distance of 79.86 pc (GDR2) the resulting X-ray luminosity of $5.72^{+0.31}_{-1.60} \times 10^{27}$ erg s $^{-1}$ is a factor 7 lower than the value reported by S16.

3.12. WASP-29

WASP-29 is not significantly detected by XMM. We derive a 3σ upper limit of 0.47×10^{-14} erg cm $^{-2}$ s $^{-1}$. Based on the same observation dos Santos et al. (2021) found a more stringent upper limit, of 3.68×10^{-16} erg cm $^{-2}$ s $^{-1}$. At a distance of 87.60 pc (GDR2) we obtain an X-ray luminosity (limit) of $\lesssim 4.32 \times 10^{27}$ erg s $^{-1}$.

3.13. WASP-69

Based on the archival XMM observation we measure a flux of $6.02^{+0.27}_{-0.20} \times 10^{-14}$ erg cm $^{-2}$ s $^{-1}$, higher than the flux measured by Nortmann et al. (2018) ($4.79^{+0.15}_{-0.16} \times 10^{-14}$ erg cm $^{-2}$ s $^{-1}$). At a distance of 49.96 pc (GDR2) the resulting X-ray luminosity is $1.80^{+0.08}_{-0.07} \times 10^{27}$ erg s $^{-1}$.

3.14. HAT-P-11 (S16)

This system was observed once with XMM and once with Chandra. For the former data set, we measure a flux of $3.25^{+0.17}_{-0.28} \times 10^{-14}$ erg cm $^{-2}$ s $^{-1}$, consistent with the value derived by K18, as well as (within the errors) with that reported by S16 on the

basis of the Pizzolato et al. (2003) relation. We also report, for the first time, on the Chandra observation (observation B in Table 2), for which we measure a flux of $7.84_{-0.72}^{+0.84} \times 10^{-14}$ erg cm⁻² s⁻¹, implying statistically significant variability over a 6 month timescale. At a distance of 37.77 pc, these measurements imply an X-ray luminosity in the range $[5.55_{-0.49}^{+0.33}-13.38_{-1.23}^{+1.44}] \times 10^{27}$ erg s⁻¹.

3.15. 55 Cnc (S16)

This system was observed once with XMM and twice with Chandra (obs. A, B and C, respectively). For observation A, we derive a flux of $8.65_{-1.96}^{+0.71} \times 10^{-14}$ erg cm⁻² s⁻¹, in agreement within the errors with the analysis of Poppenhaeger et al. (2010), and a factor about 3.6 times higher than estimated by Sanz-Forcada et al. (2011) and, given by S16 (2.4×10^{-14} erg cm⁻² s⁻¹). The two Chandra observations, which we report on for the first time, yield a 3 σ upper limit of $\lesssim 1.89 \times 10^{-14}$ erg cm⁻² s⁻¹ for observation B and a detection of $0.77_{-0.19}^{+0.32} \times 10^{-14}$ erg cm⁻² s⁻¹ for observation C, implying significant variability. At a distance of 12.59 pc (GDR2), this implies an X-ray luminosity in the range $[\lesssim 3.59 \text{ s}^{-1}-1.46_{-0.36}^{+0.61}-16.41_{-3.70}^{+1.41}] \times 10^{26}$ erg s⁻¹.

3.16. HD 97658 (S16)

This target was observed once with XMM (observation A in Table 2) and three times with Chandra (B, C and D). For the XMM observation we measure an X-ray flux of $3.20_{-0.78}^{+0.06} \times 10^{-14}$ erg s⁻¹ cm⁻², consistent within the errors with the analysis of Bourrier et al. (2017) and K18, as well as with the value quoted by S16 on the basis of the empirical relation between L_X , stellar rotation period, and stellar mass obtained by (Pizzolato et al. 2003). Analysis of the three Chandra observations confirms the presence of variability Bourrier et al. (2017); we measure X-ray fluxes of $[1.73_{-0.75}^{+0.61}-0.98_{-0.51}^{+0.35}-\lesssim 1.32] \times 10^{-14}$ erg cm⁻² s⁻¹ for the B/C/D observations, respectively. At a distance of 21.56 pc (GDR2), combining the XMM and Chandra results we derive an X-ray luminosity in the range $[0.55 \pm 0.30-1.78_{-0.43}^{+0.03}] \times 10^{27}$ erg s⁻¹.

3.17. WASP-107

Based on the archival XMM observation we measure a flux of $1.42_{-0.02}^{+0.01} \times 10^{-14}$ erg cm⁻². This is 2.5 times lower than estimated by Nortmann et al. (2018) based on the same data. At a distance of 64.74 pc (GDR2) we derive an X-ray luminosity of $7.12 \pm 0.05 \times 10^{27}$ erg s⁻¹.

3.18. HD 219134

Based on the archival XMM observation, which we analyze for the first time, we obtain a flux of $18.07_{-0.89}^{+0.40} \times 10^{-14}$ erg cm⁻². At a distance of 6.53 pc (GDR2) we derive an X-ray luminosity of $9.22_{-0.46}^{+0.20} \times 10^{26}$ erg s⁻¹.

3.19. GJ 9827

This system was observed three times with XMM (A,B,C). We analyze these observations for the first time, yielding a flux of $[0.68_{-0.12}^{+0.13}-0.65_{-0.15}^{+0.10}-0.43_{-0.09}^{+0.15}]$ for observation A/B/C, respec-

tively. At a distance of 29.66 pc, these measurements imply an X-ray luminosity in the range $[4.53_{-0.95}^{+1.58}-7.16_{-2.64}^{+1.37}] \times 10^{26}$ erg s⁻¹.

3.20. K2-25

Based on the archival XMM observation we obtain a flux of $8.61_{-0.45}^{+0.50} \times 10^{-14}$ erg cm⁻², consistent within the errors with the value reported in Rockcliffe et al. (2021) based on the same observation. At a distance of 44.96 pc (GDR2) we derive an X-ray luminosity of $2.08_{-0.12}^{+0.13} \times 10^{28}$ erg s⁻¹.

3.21. GJ 436 (S16)

This system has eight archival observations, two with XMM (obs A and H) and 6 with Chandra (obs. B-G). For the XMM data we derive fluxes of $2.37_{-0.54}^{+0.15}$ and $2.93_{-0.33}^{+0.20} \times 10^{-14}$ erg cm⁻² s⁻¹ respectively for obs. A and H, both in excellent agreement with the values reported by K18. However our obs. A flux is 4 times higher than that measured by Sanz-Forcada et al. (2011) (and given by S16) and 1.7 lower than that estimated by Ehrenreich et al. 2015. We also analyzed the 6 Chandra observations, for which we estimate fluxes of $[2.29_{-1.79}^{+0.26}-1.80_{-0.45}^{+0.33}-1.60_{-0.36}^{+0.22}-1.97_{-0.43}^{+0.37}-1.79_{-0.63}^{+0.34}-2.86_{-0.50}^{+0.53}] \times 10^{-14}$ erg cm⁻² s⁻¹ for B/C/D/E/F/G respectively. At a distance of 9.75 pc (GDR2) our fluxes imply an X-ray luminosity in the range $[1.82_{-0.41}^{+0.25}-3.33_{-0.61}^{+0.23}] \times 10^{26}$ erg s⁻¹.

3.22. LHS1140

We report on the analysis of the XMM observation of this target for the first time. We measure an X-ray flux of $0.50_{-0.08}^{+0.07} \times 10^{-14}$ erg cm⁻² s⁻¹, consistent with the upper limit reported by Spinelli et al. (2019) based on a Swift telescope observation. At a distance of 14.99 pc (GDR2) we derive an X-ray luminosity of $1.34_{-0.21}^{+0.19} \times 10^{26}$ erg s⁻¹.

3.23. AU Mic

AU Mic was observed five times with XMM (obs A-E). We measure fluxes between $[2209 \pm 4 - 3164_{-5}^{+4}] \times 10^{-14}$ erg cm⁻² s⁻¹. At a distance of 9.72 pc (GDR2) these imply an X-ray luminosity in the range $[2.498_{-0.005}^{+0.004}-3.577_{-0.006}^{+0.005}] \times 10^{29}$ erg s⁻¹.

3.24. GJ 3470 (S16)

Based on the XMM observation on this target we measure a flux of $3.68_{-0.25}^{+0.31} \times 10^{-14}$ erg cm⁻² s⁻¹, consistent within the errors with the value measured by K18 based on the same observation. Based of the Pizzolato et al. (2003) relation, S16 give 4.24×10^{-14} erg cm⁻² s⁻¹. At a distance of 29.42 (GDR2) our flux implies an X-ray luminosity of $3.81_{-0.26}^{+0.32} \times 10^{27}$ erg s⁻¹.

3.25. GJ 1214 (S16)

This system was observed once with XMM (obs A) and once with Chandra (obs B). For the XMM data, we derive a flux of $0.62_{-0.05}^{+0.27} \times 10^{-14}$ erg cm⁻² s⁻¹, formally inconsistent with the value reported by Lalitha et al. (2014) and used by S16 (the difference arise in the choice of the best-fit model; we use a two

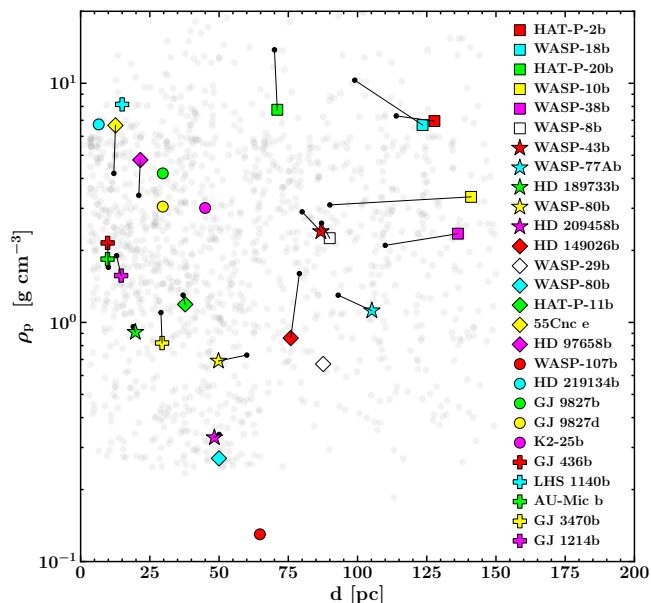


Fig. 3. Revised densities for the planet sample under consideration as a function of the Gaia DR2 distances. When applicable, these are compared to the values adopted by S16 (black dots). The grey circles in the background illustrate all the known planets within 150 pc.

temperature APEC model with coronal temperatures free to vary between 0.01–2.00 keV, whereas [Lalitha et al. 2014](#) assumed a single temperature APEC model). For the Chandra observation we found an upper limit of $\lesssim 0.32 \times 10^{-14}$ erg cm $^{-2}$ s $^{-1}$. At a distance of 16.79 pc (GDR2), this translates into a luminosity range of $\lesssim 1.08\text{--}2.09_{-0.17}^{+0.91} \times 10^{26}$ erg s $^{-1}$.

3.26. HD 189733 (S16)

Because of the large number of pointings available, the observations for this system are listed in a separate table, i.e. Table 3. The flux quoted by S16 refers to the work of [Sanz-Forcada et al. \(2011\)](#), based on the first observation of the system, with XMM. For the same observation (A), we measure a flux of $3.35 \pm 0.07 \times 10^{-13}$ erg cm $^{-2}$ s $^{-1}$, in excellent agreement with [Sanz-Forcada et al. \(2011\)](#). In addition, we perform a re-analysis of 30 other archival observations – 24 more with XMM-Newton, and 6 with Chandra – taken between 2007 and 2015. We confirm that the system exhibits statistically significant X-ray variability, between $[2.78_{-0.10}^{+0.08}\text{--}5.68_{-0.07}^{+0.06}] \times 10^{-13}$ erg cm $^{-2}$ s $^{-1}$, in broad agreement with [Pillitteri et al. \(2022\)](#) (XMM) and [Poppenhaeger et al. \(2010\)](#) (Chandra). At a distance of 19.76 pc (GDR2), this yields a luminosity range between $[1.30_{-0.05}^{+0.04}\text{--}2.65 \pm 0.03] \times 10^{28}$ erg s $^{-1}$.

4. Planetary parameters

Reliable estimates of planetary parameters require accurate measurements of the host star properties. In this section we describe how we use the parallactic distances from GDR2 to yield revised estimates of planetary radii R_p , masses M_p , and orbital separa-

tions a . As noted above, all systems under consideration have both transit and radial velocity measurements.

The first step consists of estimating the stellar density ρ_* . For circular orbits, ρ_* can be obtained directly from the photometric transit data, namely the total transit duration, T ; the duration of the "flat part" of the transit, t_F (between the so-called second and the third contacts); the orbital period, P ; and the transit depth ΔF . These yield the ratio between the orbital semi-major axis a and the stellar radius R_* ([Seager & Mallén-Ornelas 2003](#)):

$$\left(\frac{a}{R_*}\right) = \left[\frac{(1 + \sqrt{\Delta F})^2 - b^2(1 - \sin^2 \xi)}{\sin^2 \xi}\right]^{1/2}, \quad (1)$$

where

$$b = \left[\frac{(1 - \sqrt{\Delta F})^2 - \Sigma(1 + \sqrt{\Delta F})^2}{1 - \Sigma}\right]^{1/2},$$

and

$$\xi = \frac{T\pi}{P}, \quad \kappa = \frac{t_F\pi}{P}, \quad \Sigma = \frac{\sin^2 \kappa}{\sin^2 \xi}.$$

Under the assumption $M_p \ll M_*$ (M_* being the stellar mass), Kepler's Third Law can be written as:

$$\rho_* \simeq \frac{3\pi}{GP^2} \left(\frac{a}{R_*}\right)^3, \quad (2)$$

and combined with Eq. 1 to obtain ρ_* .

As shown by [Kipping \(2010\)](#); [Moorhead et al. \(2011\)](#); [Tingey et al. \(2011\)](#); [Dawson & Johnson \(2012\)](#); [Van Eylen & Albrecht \(2015\)](#), the above can be generalized to non circular orbits with known eccentricity and periastron argument (ω), e.g., from secondary transit timing, transit timing variations, or radial velocity curves. In this case we have ([Kipping 2010](#)):

$$\rho_* \simeq \frac{3\pi}{GP^2} \left(\frac{a}{R_*}\right)^3 \frac{(1 - e^2)^{3/2}}{(1 + e \sin \omega)^3} = \frac{3\pi}{GP^2} \left(\frac{a}{R_*}\right)_E^3, \quad (3)$$

where a is now the semi-major axis; $(a/R_*)_E$ denotes the eccentricity-corrected ratio.

The next step consists of breaking the degeneracy between R_* and M_* . A first approach proposed by, e.g., [Hellier et al. \(2011\)](#); [Southworth \(2010\)](#); [Bakos et al. \(2011\)](#); [McArthur et al. \(2004\)](#); [Maxted et al. \(2013\)](#), leverages stellar evolutionary models and combines distance-independent stellar parameters (such as effective temperature and metallicity) with the stellar density that is inferred from transit data to yield an estimate of mass and radius (see, e.g., [Rodríguez Martínez et al. 2021](#) for a discussion of the uncertainties at play in this method). A second approach makes use of empirical mass-luminosity relations that are calibrated using dynamical mass measurements of stellar binaries (e.g., [Butler et al. 2004](#); [Bonfils et al. 2012](#)), under the assumption that the main stellar properties are not altered by the presence of a companion. A third approach, recently proposed by [Stassun et al. \(2017\)](#), consists of estimating R_* of a star with known bolometric flux, effective temperature and distance from Stefan-Boltzmann's law.

For the FGK stars in our sample, we make use of the radius estimates derived by [Andrae et al. \(2018\)](#) based on GDR2 distances. For the M stars in our sample, we apply the new luminosity–temperature–radius relations that were recently derived [Morrell & Naylor \(2019\)](#) accounting for the well-known radius

Table 5. Planetary parameters after GDR2 distances; stellar density (1), stellar mass (2), planet radius (3), planet mass (4), semimajor axis (5), zero-albedo equilibrium temperature (6), X-ray irradiation (i.e., flux at the planet) (7), EUV irradiation (8), ATES mass loss rates (9), fractional mass loss, in parts per thousand per Gyr (10).

	ρ_* [ρ_\odot]	M_* [M_\odot]	R_p [R_J]	M_p [M_J]	a [AU]	T_{eq} [K]	$\log(F_X)$ (a)	$\log(F_{EUV})$ (a)	$\log(\dot{M})$ [g s^{-1}]	\dot{M}/M_p [$\% \text{Gyr}^{-1}$]
	(1)	(2)	(3)	(4)	(5)	(6)	(7)	(8)	(9)	(10)
Host FGK										
HAT-P-2 b	0.31	1.60	1.22	10.106	0.072	1495	3.76	2.97	-	-
WASP-18 b	0.64	1.22	1.23	10.03	0.020	2449	<3.21	-	-	-
HAT-P-20 b	2.38	0.93	1.10	8.312	0.039	944	3.41	3.80	-	-
WASP-10 b	2.16	0.65	1.03	2.914	0.036	1015	<3.77	-	-	-
WASP-38 b	0.51	1.62	1.20	3.272	0.083	1252	<2.81	-	-	-
WASP-8 b	1.22	1.18	1.09	2.331	0.084	930	3.20	3.47	-	-
WASP-43 b	2.49	0.72	1.02	2.044	0.015	1366	4.01	4.49	7.97	<10
WASP-77 A b	1.10	0.94	1.24	1.695	0.024	1701	4.02	4.43	9.60	<10
HD 189733 b	1.98	0.94	1.19	1.237	0.033	1183	3.65-3.92	4.02-4.19	9.78-9.99	<10
WASP-80 b	2.87	0.65	1.02	0.586	0.036	811	3.15	3.65	10.57	<10
HD 209458 b	0.73	1.20	1.40	0.720	0.048	1450	2.98	3.76	11.12	<10
HD 149026 b	0.34	1.09	0.74	0.282	0.041	1760	3.04	3.93	11.08	<10
WASP-29 b	1.70	0.92	0.79	0.264	0.047	946	<2.84	-	-	-
WASP-69 b	1.55	0.85	1.07	0.265	0.046	995	3.48	3.85	11.50	20
HAT-P-11 b	1.76	0.80	0.44	0.081	0.052	879	2.83-3.20	3.41-3.57	10.41-10.59	<10
55 Cnc e	1.08	0.93	0.17	0.026	0.016	2000	2.33-3.39	3.85-4.32	10.22-10.59	11-25
HD 97658 b	2.16	0.91	0.20	0.028	0.085	744	1.43-1.94	2.53-2.76	9.01-9.24	<10
WASP-107 b	2.17	0.85	1.03	0.111	0.059	717	2.86	3.37	11.35	33
HD 219134 b	1.62	0.84	0.14	0.015	0.039	1046	2.33	3.32	9.61	<10
GJ 9827 b	2.67	0.73	0.15	0.012	0.020	1147	2.80	3.76	10.17	20
GJ 9827 d	2.67	0.73	0.20	0.018	0.060	665	1.86	2.81	9.42	<10
Host M										
K2-25 b	10.37	0.35	0.34	0.094	0.032	494	3.79	3.72	10.44	<10
GJ 436 b	5.90	0.47	0.35	0.072	0.029	634	1.87-2.13	2.97-3.08	9.71-9.79	<10
LHS 1140 b	19.65	0.18	0.14	0.019	0.094	217	0.73	1.56	7.72	<10
AU Mic b	1.31	0.30	0.30	0.038	0.055	646	4.46-4.63	4.14-4.22	11.18-11.29	66-85
GJ 3470 b	3.27	0.54	0.41	0.045	0.036	706	3.03	3.56	10.65	16
GJ 1214 b	16.79	0.17	0.25	0.019	0.015	560	2.42	3.24	10.09	11

inflation (compared to theoretical models) in such stars (e.g. Birkby et al. 2012; Stassun et al. 2012; Mann et al. 2015; Somers & Stassun 2017).

Once the stellar radius and mass are known, the depth of the transit gives the (optical) planetary radius R_p . Finally, if $M_p \ll M_*$, M_p is estimated through RV techniques (Torres et al. 2008) as:

$$\frac{M_p \sin i}{M_J} = 4.919 \times 10^{-3} \left(\frac{K}{\text{m/s}} \right) (1-e^2)^{1/2} \left(\frac{P}{\text{days}} \right)^{1/3} \left(\frac{M_*}{M_\odot} \right)^{2/3} \quad (4)$$

where i is the orbital inclination angle with respect to the line of sight and K the radial velocity semi-amplitude.

The revised planetary parameters for our sample are listed in Table 5; planetary densities are shown as red circles in Figure 3 as a function of the GDR2 distances.

Worth mentioning is the case of the HD 149026 b, for which we derive a density of $0.86 \pm 0.09 \text{ g cm}^{-3}$ – a factor of two lower than assumed by S16 – in excellent agreement with the value reported by Carter et al. (2009) ($0.85 \pm 0.1 \text{ g cm}^{-3}$) and Bonomo et al. (2017) ($0.75 \pm 0.08 \text{ g cm}^{-3}$) on the basis of stellar evolution models. This new estimate, which arises from the combination of a smaller planetary mass ($0.28 M_J$ vs. $0.36 M_J$) and larger planetary radius ($0.74 R_J$ vs. $0.65 R_J$), means that HD

149026 b is not unusually dense, and thus does not warrant especially high metallicities (see, e.g., Sato et al. 2005; Fortney et al. 2006; Broeg & Wuchterl 2007).

Other notable difference with respect to the densities reported by S16 are HAT-P-20 b, for which we infer $7.75 \pm 2.43 \text{ g cm}^{-3}$, in agreement with Esposito et al. (2017) and Sun et al. (2017); WASP-18 b, for which we infer $6.70 \pm 1.73 \text{ g cm}^{-3}$, and 55 Cnc, for which we derive $6.67 \pm 1.49 \text{ g cm}^{-3}$.

A discussion of how the revised planetary parameters impact the ensuing mass loss rates is deferred to § 6.

5. Mass loss rates

Mass loss rates are calculated using the 1D photoionization hydrodynamics code ATES⁵ (Caldiroli et al. 2021, Paper I of this series). ATES computes the temperature, density, velocity and ionization fraction profiles of a highly irradiated planetary atmosphere, and estimates the ensuing steady-state mass loss rate under the assumption of a primordial atmosphere (entirely composed of atomic hydrogen and helium). As inputs we adopt the relevant parameters listed in Table 1 and 4, and specifically: stel-

⁵ The code is publicly available at <https://github.com/AndreaCaldiroli/ATES-Code>.

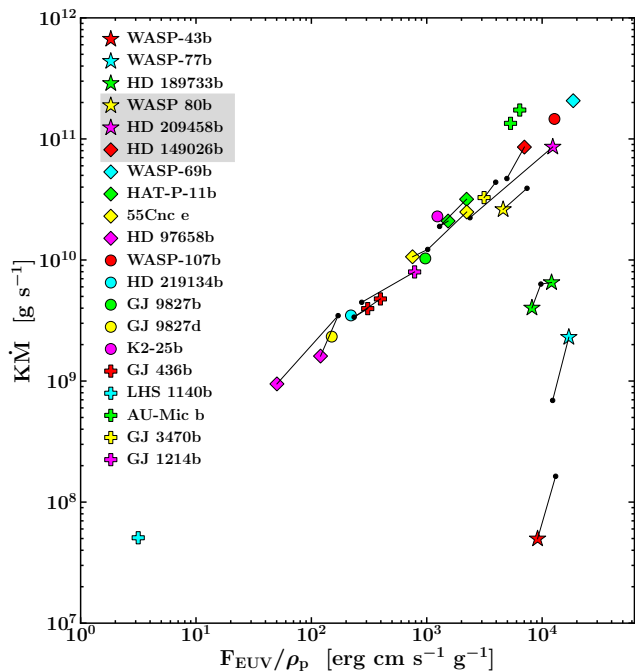


Fig. 4. K -reduced mass outflow rates ($K\dot{M}$) obtained with ATES, plotted as a function of the planetary density to irradiation ratio (F_{EUV}/ρ_p) for the planet sample under consideration. For those cases that were also considered by S16, we compare the outflow rates derived with the new (GDR2) planetary parameters (color symbols) to those derived based on the “old” values (black dots). Systems with two symbols represent those whose host star exhibits X-ray variability. The gray stripe in the legend highlights intermediate gravity planets (see Figure 5).

lar mass, planetary radius and mass, (eccentricity-corrected) average orbital distance, and planet equilibrium temperature.

Lacking a direct measurement, we estimate the EUV irradiation experienced by the planet using the (revised) inferred stellar X-ray luminosities and orbital separations, as follows.

For planets with zero eccentricity (or with eccentricity upper limits) we adopt the semi-major axis reported in Table 5; for non-zero eccentricity planets we use the time-averaged orbital separation defined by Williams (2003). In the case of K2-25 b ($e = 0.43$) and HAT-P-2 b ($e = 0.52$) the time-averaged separation is larger than the semi-major axis value by about 9% and 13%, respectively; this implies a decrease in the time-averaged flux experienced by the planet of 16% and 22%, respectively.

Since we are interested in realistic mass loss rate estimates (more so than limits), we run ATES only for those (23 out of 27) planets whose host stars have a statistically significant X-ray detection (22 out of 26). In those cases where X-ray variability is seen, we report the corresponding minimum and maximum mass loss value. As expected based on the convergence study discussed in Caldiroli et al. (2021), ATES fails to converge for the three highest-gravity planets in the sample, namely HAT-P-20 b, WASP-8 b and HAT-P-2⁶. In summary, we derive revised/new

⁶ The converge study shows that ATES recovers stable, steady-state solutions for systems with $\log(-\Phi_p) \lesssim 12.9 + 0.17 \log F_{\text{XUV}}$, where Φ_p and F_{XUV} are the planet gravitational potential and stellar irradiance in cgs units.

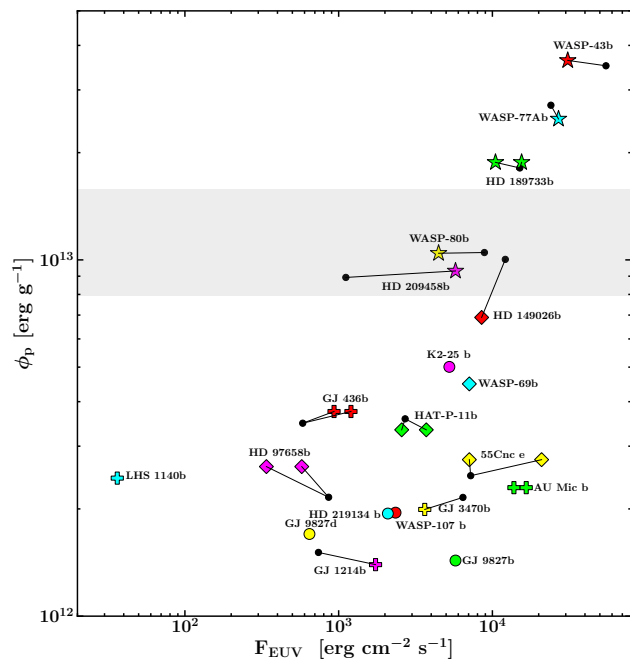


Fig. 5. Gravitational potential ϕ_p as a function of the EUV irradiation for the planet sample under consideration. For those cases that we also considered by S16, we compare ϕ_p and F_{EUV} derived with the new (after GDR2) parameters (color symbols) to those derived based on the “old” values (black dots). The gray stripe in the legend highlights intermediate gravity planets, with ϕ_p between $\sim 8 - 14 \times 10^{12} \text{ erg g}^{-1}$.

mass loss rates estimates for a total of 20 planets. The results are listed in Table 5 and shown in Figure 4.

6. Discussion

Figure 4 and 5 summarize our results. Following Caldiroli et al. (2021), Figure 4 shows the K -reduced⁷ mass loss rates ($K\dot{M}$) calculated by ATES as a function of the irradiation to planetary density ratio (F_{XUV}/ρ_p) for our sample. Figure 5 elucidates the role of planetary gravity (here defined as $\phi_p \equiv GM_p/R_p$) on the physics of the mass loss (the lack of systems at low ϕ_p and low F_{XUV} is due to our selection criteria). For those systems that were also considered by S16, in these figures we show if/how any changes in the planetary parameters affect the ensuing mass loss rates. We do so by comparing the $K\dot{M}$ obtained by ATES using the new/revised parameters (color symbols) vs. using the “old” values, i.e. those adopted in S16, as well as Paper I of this series (black points; the reader is referred to Paper I of this series for a direct comparison between the results obtained by ATES and those obtained by The Pluto-Cloudy Interface used by S16).

As shown by Caldiroli et al. (2022), the efficiency of the atmospheric evaporation process is set primarily by the planet’s gravity; specifically, there exists a gravitational potential threshold ($\phi_p \gtrsim 14 \times 10^{12} \text{ erg g}^{-1}$) above which a planetary atmosphere can not lose mass in the energy-limited regime (e.g. Erkaev et al. 2007, and references therein), whereby virtually

⁷ this term accounts for the gravitational pull of the star; see equation 17 in Erkaev et al. 2007.

all of the absorbed stellar radiation is converted into outward mechanical work. This is because, for these systems, no matter how high F_{XUV} is, the mean kinetic energy acquired by the ions through photo-electron collisions in the atmosphere is insufficient for escape.

Conversely, for low-gravity planets (with $\phi_p \lesssim 8 \times 10^{12}$ erg g⁻¹) the mass loss rate is largely independent of ϕ_p , and is regulated primarily by F_{XUV} . Below a critical irradiation level⁸ $F_{\text{XUV}} \lesssim 10^5$ erg cm⁻² s⁻¹, low-gravity planets are expected to exhibit energy-limited outflows, in which case \dot{M} is directly proportional to the ratio F_{XUV}/ρ_p (i.e., $\sim 100\%$ efficiency). Indeed, all the low-gravity planets in our sample (below the grey stripe in Figure 5) experience irradiating fluxes below $\lesssim 10^5$ erg cm⁻² s⁻¹, meaning that any changes in F_{XUV} make the resulting \dot{M} increase or decrease along the $\dot{M} \propto (F_{\text{XUV}}/\rho_p)$ line.

The behavior is very different for the three high-gravity planets ($\phi_p \gtrsim 14 \times 10^{12}$ erg g⁻¹; above the grey stripe in Figure 5 and bottom right corner in Figure 4). Here, most of the absorbed stellar flux is dissipated locally in the form of radiative cooling, and the outflows are highly inefficient, i.e., very low \dot{M} . Unlike for low-gravity planets, the outflow efficiency plummets with increasing ϕ_p , implying that even small variations in ϕ_p lead to large changes in the mass loss rate. This is indeed the case for WASP 77 b, WASP 43 b and HD 189733 b, which, in spite of the small variations in ϕ_p (top right corner in Figure 5), all experience large changes in \dot{M} (Figure 4).

The behaviour of intermediate gravity planets (WASP-80 b, HD 149026 b, HD 209458 b, within the grey stripe in Figure 5) is indeed intermediate, and if anything more typical of low-gravity planets at high irradiation. The revised density for both WASP-80 and HD 209458 is very close to the old (S16) values, whereas it has halved for HD 149026 b. Meanwhile, the revised F_{XUV} has changed significantly (decreased by a factor 8) only for HD 149026 b. Perhaps surprisingly, these changes combine to yield an increase in the outflow rate for this system. This is because the new, lower density implies that this planet moves from the intermediate gravity regime to the low-gravity one, where the efficiency of the outflow increases with decreasing flux (Caldirola et al. 2022).

We conclude with a note on the importance of accurate F_{XUV} measurements for the purpose of estimating realistic outflow rates. In Figure 6 we overlay our X-ray measurements⁹ to the known relation between the stellar X-ray to bolometric luminosity ratio (L_X/L_{bol}) and the Rossby number (R_0) (Wright et al. 2018) (after Wright & Drake 2016 and Wright et al. 2011). This study, which includes fully convective stars, confirmed that very fast rotators ($R_0 < 0.13$) reach a saturation level of $L_X/L_{\text{bol}} \simeq 10^{-3}$, while the X-ray bolometric ratio decreases with a power law behaviour for $R_0 > 0.13$ (non-saturated regime).

Our measurements are fully consistent with the W18 relation and – more importantly – with its large scatter, which means that

⁸ This is approximately the threshold above which Lyman-alpha cooling dominates over adiabatic and advective cooling; Caldirola et al. 2022.

⁹ Where we applied the K18 relations to convert the measured X-ray luminosities into the ROSAT energy band; adopted the bolometric luminosities estimated by Andrae et al. (2018) for FGK stars, and; used the relation of Morrell & Naylor (2019) to estimate L_{bol} for M dwarfs (using GDR2 distances). To calculate the convective turnover time which enters into the expression for the Rossby number, we used the polynomial relationship given by Wright et al. (2018).

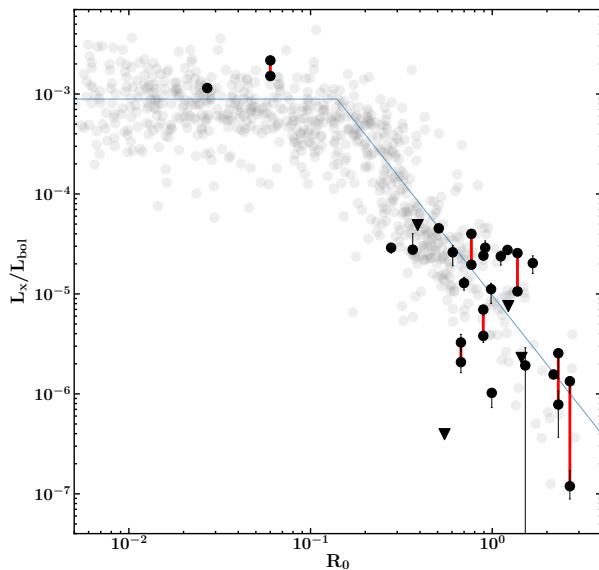


Fig. 6. Stellar X-ray to bolometric luminosity ratio as a function of Rossby number, from W18. The full W18 sample is shown in grey, with their best-fitting relation in blue, while the black dots/triangles refer to our target sample (triangles indicate upper limits). The red segments connect different measurements in the case of X-ray variable stars.

inferring the stellar L_X on the basis of properties such as rotation and convection alone can lead to exceedingly large errors (up to two orders of magnitude) in the resulting atmospheric mass loss rates. In addition, a non negligible fraction of our sample stars (HD 97658, HD 189733, HAT-P-11, 55 Cnc, GJ 436, Au Mic) exhibit significant X-ray variability (up to 225%), which can further impact the resulting mass outflows (up to 135%). Integrated over the system lifetime, these uncertainties could make the difference between retaining vs. losing the atmosphere. Additionally, large uncertainties in the inferred instantaneous mass loss rate impact our ability to reliably predict any atmospheric absorption feature during transit. As an example, by means of hydrodynamics simulations Zhang et al. (2022) conclude that $\sim 30\%$ level XUV variability can change the depth of the metastable helium absorption feature at 1,083 nm (Oklopčić & Hirata 2018) by 60% in HD 189733 b (for which we actually measure X-ray variability at the $\sim 60\%$ level). The problem is further exacerbated by the large uncertainties in the conversion from X-rays (or Lyman α) to EUV flux, whose effects are seldom discussed. This will be the subject of a forthcoming paper.

References

- Akaike, H. 1974, IEEE Transactions on Automatic Control, 19, 716
Alonso-Floriano, F. J., Snellen, I. A. G., Czesla, S., et al. 2019, A&A, 629, A110
Anderson, D. R., Collier Cameron, A., Delrez, L., et al. 2014, MNRAS, 445, 1114
Anderson, D. R., Collier Cameron, A., Delrez, L., et al. 2017, A&A, 604, A110
Andrae, R., Fouesneau, M., Creevey, O., et al. 2018, A&A, 616, A8
Anglada-Escudé, G., Rojas-Ayala, B., Boss, A. P., Weinberger, A. J., & Lloyd, J. P. 2013, A&A, 551, A48
Arnaud, K. A. 1996, in Astronomical Society of the Pacific Conference Series, Vol. 101, Astronomical Data Analysis Software and Systems V, ed. G. H. Jacoby & J. Barnes, 17
Asplund, M., Grevesse, N., Sauval, A. J., & Scott, P. 2009, ARA&A, 47, 481
Bakos, G. Á., Hartman, J., Torres, G., et al. 2011, ApJ, 742, 116

- Bakos, G. Á., Kovács, G., Torres, G., et al. 2007, *ApJ*, 670, 826
- Bakos, G. Á., Torres, G., Pál, A., et al. 2010, *ApJ*, 710, 1724
- Barros, S. C. C., Boué, G., Gibson, N. P., et al. 2013, *MNRAS*, 430, 3032
- Biddle, L. I., Pearson, K. A., Crossfield, I. J. M., et al. 2014, *MNRAS*, 443, 1810
- Birkby, J., Nefs, B., Hodgkin, S., et al. 2012, *MNRAS*, 426, 1507
- Bonfils, X., Gillon, M., Udry, S., et al. 2012, *A&A*, 546, A27
- Bonomo, A. S., Desidera, S., Benatti, S., et al. 2017, *VizieR Online Data Catalog*, J/A+A/602/A107
- Bouchy, F., Udry, S., Mayor, M., et al. 2005, *A&A*, 444, L15
- Bourrier, V., Dumusque, X., Dorn, C., et al. 2018, *A&A*, 619, A1
- Bourrier, V., Ehrenreich, D., King, G., et al. 2017, *A&A*, 597, A26
- Broeg, C. & Wuchterl, G. 2007, *MNRAS*, 376, L62
- Butler, R. P., Vogt, S. S., Marcy, G. W., et al. 2004, *ApJ*, 617, 580
- Caldirolì, A., Haardt, F., Gallo, E., et al. 2021, *A&A*, 655, A30
- Caldirolì, A., Haardt, F., Gallo, E., et al. 2022, *A&A*, 663, A122
- Carleo, I., Youngblood, A., Redfield, S., et al. 2021, *AJ*, 161, 136
- Carter, J. A., Winn, J. N., Gilliland, R., & Holman, M. J. 2009, *ApJ*, 696, 241
- Casasayas-Barris, N., Palte, E., Nowak, G., et al. 2017, *A&A*, 608, A135
- Cash, W. 1979, *ApJ*, 228, 939
- Cegla, H. M., Lovis, C., Bourrier, V., et al. 2016, *A&A*, 588, A127
- Charbonneau, D., Berta, Z. K., Irwin, J., et al. 2009, *Nature*, 462, 891
- Charbonneau, D., Brown, T. M., Latham, D. W., & Mayor, M. 2000, *ApJ*, 529, L45
- Charbonneau, D., Winn, J. N., Latham, D. W., et al. 2006, *ApJ*, 636, 445
- Christian, D. J., Gibson, N. P., Simpson, E. K., et al. 2009, *MNRAS*, 392, 1585
- Cortés-Zuleta, P., Rojo, P., Wang, S., et al. 2020, *A&A*, 636, A98
- Czesla, S., Salz, M., Schneider, P. C., & Schmitt, J. H. M. M. 2013, *A&A*, 560, A17
- Dawson, R. I. & Johnson, J. A. 2012, *ApJ*, 756, 122
- Deming, D., Knutson, H., Kammer, J., et al. 2015, *ApJ*, 805, 132
- Dittmann, J. A., Irwin, J. M., Charbonneau, D., et al. 2017, *Nature*, 544, 333
- dos Santos, L. A., Bourrier, V., Ehrenreich, D., et al. 2021, *A&A*, 649, A40
- Dragomir, D., Matthews, J. M., Eastman, J. D., et al. 2013, *ApJ*, 772, L2
- Edwards, B., Changeat, Q., Mori, M., et al. 2021, *AJ*, 161, 44
- Ehrenreich, D., Bourrier, V., Bonfils, X., et al. 2012, *A&A*, 547, A18
- Ehrenreich, D., Bourrier, V., Wheatley, P. J., et al. 2015, *Nature*, 522, 459
- Ellis, T. G., Boyajian, T., von Braun, K., et al. 2021, *AJ*, 162, 118
- Erkaev, N. V., Kulikov, Yu. N., Lammer, H., et al. 2007, *A&A*, 472, 329
- Erkaev, N. V., Lammer, H., Odert, P., et al. 2016, *MNRAS*, 460, 1300
- Erkaev, N. V., Lammer, H., Odert, P., et al. 2013, *Astrobiology*, 13, 1011, pMID: 24251443
- Esposito, M., Covino, E., Desidera, S., et al. 2017, *A&A*, 601, A53
- Folsom, C. P., Fossati, L., Wood, B. E., et al. 2018, *MNRAS*, 481, 5286
- Fortney, J. J., Saumon, D., Marley, M. S., Lodders, K., & Freedman, R. S. 2006, *ApJ*, 642, 495
- Fossati, L., Guilluy, G., Shaikhislamov, I. F., et al. 2022, *A&A*, 658, A136
- Fulton, B. J., Petigura, E. A., Howard, A. W., et al. 2017, *AJ*, 154, 109
- Gaia Collaboration, Brown, A. G. A., Vallenari, A., et al. 2018, *A&A*, 616, A1
- Gehrels, N. 1986, *ApJ*, 303, 336
- Gillon, M., Triaud, A. H. M. J., Demory, B.-O., et al. 2017, *Nature*, 542, 456
- Hellier, C., Anderson, D. R., Collier Cameron, A., et al. 2009, *Nature*, 460, 1098
- Hellier, C., Anderson, D. R., Collier Cameron, A., et al. 2011, *A&A*, 535, L7
- Hellier, C., Anderson, D. R., Collier Cameron, A., et al. 2010, *ApJ*, 723, L60
- Henry, G. W., Marcy, G. W., Butler, R. P., & Vogt, S. S. 2000, *ApJ*, 529, L41
- Howard, A. W., Johnson, J. A., Marcy, G. W., et al. 2011, *ApJ*, 730, 10
- Huber, K. F., Czesla, S., & Schmitt, J. H. M. M. 2017, *A&A*, 597, A113
- Kasper, D., Bean, J. L., Oklopčić, A., et al. 2020, *AJ*, 160, 258
- Kasting, J. F., Whitmire, D. P., & Reynolds, R. T. 1993, *Icarus*, 101, 108
- King, G. W., Wheatley, P. J., Salz, M., et al. 2018, *MNRAS*, 478, 1193
- Kipping, D. M. 2010, *MNRAS*, 407, 301
- Knutson, H. A., Fulton, B. J., Montet, B. T., et al. 2014, *ApJ*, 785, 126
- Kopparapu, R. K., Hébrard, E., Belikov, R., et al. 2018, *ApJ*, 856, 122
- Kopparapu, R. K., Ramirez, R., Kasting, J. F., et al. 2013, *ApJ*, 765, 131
- Kreidberg, L., Bean, J. L., Désert, J.-M., et al. 2014, *Nature*, 505, 69
- Kulow, J. R., France, K., Linsky, J., & Loyd, R. O. P. 2014, *ApJ*, 786, 132
- Lalitha, S., Poppenhaeger, K., Singh, K. P., Czesla, S., & Schmitt, J. H. M. M. 2014, *ApJ*, 790, L11
- Lammer, H., Selsis, F., Ribas, I., et al. 2003, *ApJ*, 598, L121
- Lanotte, A. A., Gillon, M., Demory, B. O., et al. 2014, *A&A*, 572, A73
- Lavie, B., Ehrenreich, D., Bourrier, V., et al. 2017, *A&A*, 605, L7
- Lecavelier des Etangs, A., Ehrenreich, D., Vidal-Madjar, A., et al. 2010, *A&A*, 514, A72
- Li, T. P. & Ma, Y. Q. 1983, *ApJ*, 272, 317
- Lillo-Box, J., Figueira, P., Leleu, A., et al. 2020, *A&A*, 642, A121
- Linsky, J. L., Redfield, S., Wood, B. E., & Piskunov, N. 2000, *ApJ*, 528, 756
- Lopez, E. D. & Fortney, J. J. 2014, *ApJ*, 792, 1
- Luri, X., Brown, A. G. A., Sarro, L. M., et al. 2018, *A&A*, 616, A9
- Mann, A. W., Feiden, G. A., Gaidos, E., Boyajian, T., & von Braun, K. 2015, *ApJ*, 804, 64
- Mann, A. W., Gaidos, E., Mace, G. N., et al. 2016, *ApJ*, 818, 46
- Mansfield, M., Bean, J. L., Oklopčić, A., et al. 2018, *ApJ*, 868, L34
- Martoli, E., Hébrard, G., Correia, A. C. M., Laskar, J., & Lecavelier des Etangs, A. 2021, *A&A*, 649, A177
- Maxted, P. F. L., Anderson, D. R., Collier Cameron, A., et al. 2013, *PASP*, 125, 48
- McArthur, B. E., Endl, M., Cochran, W. D., et al. 2004, *ApJ*, 614, L81
- Ment, K., Dittmann, J. A., Astudillo-Defru, N., et al. 2019, *AJ*, 157, 32
- Miller, B. P., Gallo, E., Wright, J. T., & Dupree, A. K. 2012, *ApJ*, 754, 137
- Moorhead, A. V., Ford, E. B., Morehead, R. C., et al. 2011, *ApJS*, 197, 1
- Morrell, S. & Naylor, T. 2019, *MNRAS*, 489, 2615
- Motalebi, F., Udry, S., Gillon, M., et al. 2015, *A&A*, 584, A72
- Murray, A. G. 2007, *Planet. Space Sci.*, 55, 1426
- Murray-Clay, R. A., Chiang, E. I., & Murray, N. 2009, *ApJ*, 693, 23
- Nortmann, L., Pallé, E., Salz, M., et al. 2018, *Science*, 362, 1388
- Nutzman, P., Charbonneau, D., Winn, J. N., et al. 2009, in *Transiting Planets*, ed. F. Pont, D. Sasselov, & M. J. Holman, Vol. 253, 466–469
- Oklopčić, A. 2019, *ApJ*, 881, 133
- Oklopčić, A. & Hirata, C. M. 2018, *ApJ*, 855, L11
- Orell-Miquel, J., Murgas, F., Pallé, E., et al. 2022, *A&A*, 659, A55
- Owen, J. E. 2019, *ARA&A*, 47, 67
- Owen, J. E. & Jackson, A. P. 2012, *MNRAS*, 425, 2931
- Owen, J. E. & Lai, D. 2018, *MNRAS*, 479, 5012
- Owen, J. E. & Wu, Y. 2013, *ApJ*, 775, 105
- Palle, E., Nortmann, L., Casasayas-Barris, N., et al. 2020, *A&A*, 638, A61
- Petit dit de la Roche, D. J. M., van den Ancker, M. E., & Miles-Paez, P. A. 2020, *Research Notes of the American Astronomical Society*, 4, 231
- Piaulet, C., Benneke, B., Rubenzahl, R. A., et al. 2021, *AJ*, 161, 70
- Pillitteri, I., Micela, G., Maggio, A., Sciortino, S., & Lopez-Santiago, J. 2022, arXiv e-prints, arXiv:2201.12149
- Pillitteri, I., Wolk, S. J., Cohen, O., et al. 2010, *ApJ*, 722, 1216
- Pizzolato, N., Maggio, A., Micela, G., Sciortino, S., & Ventura, P. 2003, *A&A*, 397, 147
- Playchan, P., Barclay, T., Gagné, J., et al. 2020, *Nature*, 582, 497
- Poppenhaeger, K., Röhrade, J., & Schmitt, J. H. M. M. 2010, *A&A*, 515, A98
- Queloz, D., Anderson, D. R., Collier Cameron, A., et al. 2010, *A&A*, 517, L1
- Redfield, S. & Linsky, J. L. 2008, *ApJ*, 673, 283
- Riello, M., De Angeli, F., Evans, D. W., et al. 2018, *A&A*, 616, A3
- Rockcliffe, K. E., Newton, E. R., Youngblood, A., et al. 2021, *AJ*, 162, 116
- Rodriguez, J. E., Vanderburg, A., Eastman, J. D., et al. 2018, *AJ*, 155, 72
- Rodríguez Martínez, R., Stevens, D. J., Gaudi, B. S., et al. 2021, *ApJ*, 911, 84
- Rosenthal, L. J., Fulton, B. J., Hirsch, L. A., et al. 2021, *ApJS*, 255, 8
- Saha, S. & Sengupta, S. 2021, *AJ*, 162, 221
- Salz, M., Banerjee, R., Mignone, A., et al. 2015, *A&A*, 576, A21
- Salz, M., Czesla, S., Schneider, P. C., et al. 2018, *A&A*, 620, A97
- Salz, M., Czesla, S., Schneider, P. C., & Schmitt, J. H. M. M. 2016, *A&A*, 586, A75
- Salz, M., Schneider, P. C., Czesla, S., & Schmitt, J. H. M. M. 2016, *A&A*, 585, L2
- Sanz-Forcada, J., Micela, G., Ribas, I., et al. 2011, *A&A*, 532, A6
- Sartoretti, P., Katz, D., Cropper, M., et al. 2018, *A&A*, 616, A6
- Sato, B., Fischer, D. A., Henry, G. W., et al. 2005, *ApJ*, 633, 465
- Seager, S. & Mallén-Ornelas, G. 2003, *ApJ*, 585, 1038
- Simpson, E. K., Pollacco, D., Cameron, A. C., et al. 2011, *MNRAS*, 414, 3023
- Somers, G. & Stassun, K. G. 2017, *AJ*, 153, 101
- Southworth, J. 2010, *MNRAS*, 408, 1689
- Spake, J. J., Sing, D. K., Evans, T. M., et al. 2018, *Nature*, 557, 68
- Spinelli, R., Borsa, F., Ghirlanda, G., et al. 2019, *A&A*, 627, A144
- Stassun, K. G., Collins, K. A., & Gaudi, B. S. 2017, *AJ*, 153, 136
- Stassun, K. G., Kratter, K. M., Scholz, A., & Dupuy, T. J. 2012, *ApJ*, 756, 47
- Steffansson, G., Mahadevan, S., Maney, M., et al. 2020, *AJ*, 160, 192
- Stevenson, K. B., Harrington, J., Fortney, J. J., et al. 2012, *ApJ*, 754, 136
- Sun, L., Gu, S., Wang, X., et al. 2017, *AJ*, 153, 28
- Tian, F., Toon, O., Pavlov, A., & De Sterck, H. 2005, *ApJ*, 621, 1049
- Tingley, B., Bonomo, A. S., & Deeg, H. J. 2011, *ApJ*, 726, 112
- Torres, G., Winn, J. N., & Holman, M. J. 2008, *ApJ*, 677, 1324
- Triaud, A. H. M. J., Anderson, D. R., Collier Cameron, A., et al. 2013, *A&A*, 551, A80
- Triaud, A. H. M. J., Gillon, M., Ehrenreich, D., et al. 2015, *MNRAS*, 450, 2279
- Van Eylen, V. & Albrecht, S. 2015, *ApJ*, 808, 126
- Van Grootel, V., Gillon, M., Valencia, D., et al. 2014, *ApJ*, 786, 2
- Vidal-Madjar, A., Lecavelier des Etangs, A., Désert, J. M., et al. 2003, *Nature*, 422, 143
- Vilhu, O. 1984, *A&A*, 133, 117
- Vilhu, O. & Walter, F. M. 1987, *ApJ*, 321, 958
- Vogt, S. S., Burt, J., Meschiari, S., et al. 2015, *ApJ*, 814, 12
- von Braun, K., Boyajian, T. S., Kane, S. R., et al. 2012, *ApJ*, 753, 171
- Watson, A., Donahue, T., & Walker, J. 1981, *Icarus*, 48, 150
- Williams, D. M. 2003, *American Journal of Physics*, 71, 1198
- Wilms, J., Allen, A., & McCray, R. 2000, *ApJ*, 542, 914
- Winn, J. N., Henry, G. W., Torres, G., & Holman, M. J. 2008, *ApJ*, 675, 1531
- Wright, N. J. & Drake, J. J. 2016, *Nature*, 535, 526
- Wright, N. J., Drake, J. J., Mamajek, E. E., & Henry, G. W. 2011, *ApJ*, 743, 48
- Wright, N. J., Newton, E. R., Williams, P. K. G., Drake, J. J., & Yadav, R. K. 2018, *MNRAS*, 479, 2351
- Wu, Y. 2019, *ApJ*, 874, 91
- Wunderlich, F., Scheucher, M., Grenfell, J. L., et al. 2021, *A&A*, 647, A48
- Yee, S. W., Petigura, E. A., Fulton, B. J., et al. 2018, *AJ*, 155, 255
- Yelle, R. V. 2004, *Icarus*, 170, 167
- Zhang, M., Cauley, P. W., Knutson, H. A., et al. 2022, arXiv e-prints, arXiv:2204.02985
- Zhang, M., Knutson, H. A., Wang, L., et al. 2021, *AJ*, 161, 181

		n_H	KT_1	KT_2	KT_3	EM_1	EM_2	EM_3	F_X	
		[10^{18}cm^{-2}]	[keV]	[keV]	[keV]	[cm^{-3}]	[cm^{-3}]	[cm^{-3}]	(a)	
		(1)	(2)	(3)	(4)	(5)	(6)	(7)	(8)	
Host FGK										
	HAT-P-2	39.4	$0.32^{+0.04}_{-0.03}$	-	-	$61.96^{+11.55}_{-10.47}$	-	-	$5.50^{+0.74}_{-0.79}$	
	WASP 18	38.11	0.30	-	-	1.15	-	-	<0.10	
	HAT-P-20	22.0	$0.41^{+0.13}_{-0.01}$	-	-	$5.44^{+1.85}_{-1.48}$	-	-	$1.78^{+0.28}_{-0.35}$	
	WASP 10	43.5	0.30	-	-	1.34	-	-	<0.90	
	WASP 38	42.04	0.30	-	-	7.71	-	-	<0.56	
	WASP 8	27.8	$0.29^{+0.04}_{-0.03}$	-	-	$20.57^{+4.99}_{-4.19}$	-	-	$3.50^{+0.61}_{-0.71}$	
	WASP 43	26.8	$1.08^{+0.38}_{-0.28}$	$0.18^{+0.06}_{-0.04}$	-	$1.39^{+1.29}_{-0.75}$	$2.52^{+1.05}_{-0.87}$	-	$0.75^{+0.12}_{-0.20}$	
	WASP 77	32.6	0.75 ± 0.11	-	-	$6.60^{+1.58}_{-1.36}$	-	-	$1.24^{+0.16}_{-0.35}$	
HD 189733	A	6.1	$0.67^{+0.03}_{-0.02}$	0.20 ± 0.01	-	$2.88^{+0.19}_{-0.21}$	$4.91^{+0.17}_{-0.24}$	-	33.46 ± 0.74	
	B	6.1	$0.74^{+0.02}_{-0.01}$	0.19 ± 0.01	-	6.15 ± 0.18	6.14 ± 0.18	-	$48.84^{+0.75}_{-0.66}$	
	C	6.1	0.79 ± 0.02	0.22 ± 0.01	-	$4.17^{+0.12}_{-0.18}$	6.67 ± 0.25	-	$46.86^{+0.67}_{-0.60}$	
	D	6.1	$0.79^{+0.06}_{-0.04}$	$0.22^{+0.03}_{-0.02}$	-	$3.41^{+0.29}_{-0.37}$	$4.69^{+0.45}_{-0.43}$	-	$33.59^{+1.00}_{-1.37}$	
	E	6.1	0.71 ± 0.03	0.22 ± 0.02	-	$3.35^{+0.29}_{-0.30}$	$5.17^{+0.46}_{-0.44}$	-	$35.17^{+1.18}_{-1.51}$	
	F	6.1	$1.00^{+0.14}_{-0.12}$	0.28 ± 0.02	-	$1.91^{+0.20}_{-0.24}$	$6.02^{+0.52}_{-0.41}$	-	$29.72^{+1.24}_{-1.15}$	
	G	6.1	$1.40^{+0.25}_{-0.18}$	0.29 ± 0.01	-	$2.58^{+0.39}_{-0.39}$	7.81 ± 0.39	-	$34.68^{+1.53}_{-1.08}$	
	H	6.1	$1.04^{+0.10}_{-0.14}$	$0.28^{+0.01}_{-0.02}$	-	1.62 ± 0.18	$6.77^{+0.39}_{-0.49}$	-	30.64 ± 1.12	
	I	6.1	$0.75^{+0.09}_{-0.06}$	$0.23^{+0.03}_{-0.02}$	-	$2.22^{+0.36}_{-0.46}$	$4.75^{+0.58}_{-0.43}$	-	$27.84^{+0.82}_{-1.00}$	
	J	6.1	$0.75^{+0.01}_{-0.02}$	0.20 ± 0.01	-	$3.28^{+0.15}_{-0.11}$	5.32 ± 0.13	-	$37.02^{+0.60}_{-0.36}$	
	K	6.1	$0.71^{+0.03}_{-0.02}$	0.20 ± 0.01	-	$3.48^{+0.14}_{-0.22}$	5.67 ± 0.17	-	$39.36^{+0.51}_{-0.57}$	
	L	6.1	$0.75^{+0.04}_{-0.02}$	0.21 ± 0.01	-	$3.38^{+0.20}_{-0.31}$	$5.81^{+0.40}_{-0.22}$	-	$39.56^{+0.59}_{-0.76}$	
	M	6.1	$1.18^{+0.06}_{-0.03}$	0.27 ± 0.01	-	$3.25^{+0.17}_{-0.16}$	$7.91^{+0.18}_{-0.17}$	-	$41.31^{+0.60}_{-0.51}$	
	N	6.1	$0.70^{+0.02}_{-0.03}$	0.19 ± 0.01	-	$3.01^{+0.20}_{-0.19}$	5.41 ± 0.21	-	$35.80^{+0.82}_{-0.97}$	
	O	6.1	$0.71^{+0.05}_{-0.02}$	0.20 ± 0.01	-	3.68 ± 0.18	6.12 ± 0.21	-	$42.26^{+0.87}_{-0.80}$	
	P	6.1	$1.12^{+0.08}_{-0.14}$	0.27 ± 0.01	-	2.61 ± 0.15	8.16 ± 0.19	-	$40.74^{+0.61}_{-0.64}$	
	Q	6.1	$0.75^{+0.02}_{-0.01}$	0.20 ± 0.01	-	$5.01^{+0.20}_{-0.19}$	6.15 ± 0.22	-	$49.40^{+0.81}_{-0.70}$	
	R	6.1	$0.88^{+0.02}_{-0.06}$	$0.23^{+0.01}_{-0.02}$	-	$3.78^{+0.34}_{-0.18}$	$7.21^{+0.28}_{-0.54}$	-	$45.69^{+0.77}_{-0.75}$	
	S	6.1	$0.75^{+0.05}_{-0.02}$	0.20 ± 0.01	-	$4.15^{+0.16}_{-0.43}$	$5.74^{+0.48}_{-0.19}$	-	$43.37^{+0.69}_{-0.74}$	
	T	6.1	$1.25^{+0.04}_{-0.09}$	0.28 ± 0.01	-	3.84 ± 0.19	8.13 ± 0.19	-	$43.51^{+0.68}_{-0.75}$	
	U	6.1	0.70 ± 0.02	0.20 ± 0.01	-	$4.71^{+0.19}_{-0.18}$	7.02 ± 0.21	-	$51.14^{+0.75}_{-0.60}$	
	V	6.1	$0.79^{+0.04}_{-0.02}$	0.21 ± 0.01	-	$4.27^{+0.15}_{-0.26}$	$5.80^{+0.33}_{-0.18}$	-	$43.87^{+0.70}_{-0.44}$	
	W	6.1	$1.06^{+0.08}_{-0.12}$	0.28 ± 0.01	-	$2.39^{+0.16}_{-0.15}$	6.61 ± 0.21	-	$33.16^{+0.53}_{-0.55}$	
	X	6.1	$0.94^{+0.03}_{-0.06}$	0.24 ± 0.01	-	$3.50^{+0.16}_{-0.15}$	$7.02^{+0.28}_{-0.47}$	-	$42.75^{+0.58}_{-0.75}$	
	Y	6.1	$0.71^{+0.03}_{-0.02}$	0.20 ± 0.01	-	$4.63^{+0.20}_{-0.33}$	$6.54^{+0.35}_{-0.23}$	-	$48.97^{+0.76}_{-0.70}$	
	Z	6.1	0.75 ± 0.02	0.21 ± 0.01	-	$4.57^{+0.21}_{-0.19}$	6.86 ± 0.24	-	$49.86^{+0.72}_{-0.77}$	
	AA	6.1	0.78 ± 0.02	$0.22^{+0.01}_{-0.02}$	-	$5.24^{+0.19}_{-0.22}$	$7.80^{+0.28}_{-0.25}$	-	$56.75^{+0.57}_{-0.67}$	
	AB	6.1	$0.75^{+0.04}_{-0.02}$	0.23 ± 0.01	-	$3.62^{+0.20}_{-0.36}$	$7.19^{+0.51}_{-0.26}$	-	$46.04^{+0.51}_{-0.65}$	
	AC	6.1	0.83 ± 0.01	0.24 ± 0.01	-	$4.14^{+0.27}_{-0.19}$	$7.34^{+0.29}_{-0.28}$	-	$48.66^{+0.56}_{-0.64}$	
	AD	6.1	0.74 ± 0.02	0.20 ± 0.01	-	$4.77^{+0.18}_{-0.25}$	$6.97^{+0.28}_{-0.21}$	-	51.29 ± 0.76	
	AE	6.1	$0.74^{+0.02}_{-0.01}$	0.20 ± 0.01	-	5.00 ± 0.18	$7.27^{+0.21}_{-0.20}$	-	$53.46^{+0.72}_{-0.76}$	
	WASP-80	A	15.4	0.16 ± 0.03	0.73 ± 0.09	-	$1.75^{+0.56}_{-0.38}$	0.97 ± 0.18	-	$1.77^{+0.16}_{-0.28}$
		B	15.4	0.19 ± 0.02	$0.84^{+0.12}_{-0.10}$	-	$2.04^{+0.24}_{-0.23}$	0.67 ± 0.15	-	$1.70^{+0.11}_{-0.19}$
HD 209458	A	14.9	0.93	-	-	0.45	-	-	<0.35	
	C	14.9	0.93	-	-	0.23	-	-	<0.18	
	D	14.9	0.93	-	-	$2.75^{+1.23}_{-2.75}$	-	-	$2.25^{+1.12}_{-2.25}$	
HD 149026		23.5	$0.78^{+0.16}_{-0.11}$	$0.20^{+0.12}_{-0.17}$	-	$1.36^{+0.60}_{-0.59}$	$1.06^{+0.77}_{-0.63}$	-	$0.75^{+0.04}_{-0.21}$	
WASP 29		27.03	0.30	-	-	2.56	-	-	<0.47	
WASP 69		15.5	$0.82^{+0.05}_{-0.04}$	0.21 ± 0.02	-	$3.51^{+0.36}_{-0.35}$	$5.49^{+0.48}_{-0.44}$	-	$6.02^{+0.27}_{-0.20}$	
HAT-P-11	A	11.7	0.18 ± 0.02	$0.87^{+0.08}_{-0.07}$	-	$2.09^{+0.22}_{-0.20}$	8.79 ± 0.14	-	$3.25^{+0.17}_{-0.28}$	
	B	11.7	$0.67^{+0.11}_{-0.09}$	-	-	$5.39^{+0.77}_{-0.69}$	-	-	$7.84^{+0.84}_{-0.72}$	
55 Cnc	A	3.9	$0.62^{+0.07}_{-0.08}$	0.11 ± 0.01	-	0.15 ± 0.02	$1.11^{+0.43}_{-0.29}$	-	$8.65^{+0.71}_{-1.96}$	
	B	3.9	0.18	-	-	0.36	-	-	1.89	
	C	3.9	0.18 ± 0.03	-	-	$0.10^{+0.08}_{-0.04}$	-	-	$0.77^{+0.32}_{-0.19}$	
HD 97658	A	6.7	0.24 ± 0.01	$0.026^{+0.006}_{-0.005}$	-	0.55 ± 0.05	415^{+895}_{-313}	-	$3.20^{+0.10}_{-1.39}$	

	B	6.7	$0.22^{+0.05}_{-0.04}$	-	-	$0.61^{+0.39}_{-0.23}$	-	-	$1.73^{+0.61}_{-0.75}$
	C	6.7	$0.23^{+0.07}_{-0.05}$	-	-	$0.34^{+0.31}_{-0.16}$	-	-	$0.98^{+0.35}_{-0.51}$
	D	6.7	0.22	-	-	0.50	-	-	<1.32
WASP-107		20.0	0.10 ± 0.03	$0.31^{+0.06}_{-0.05}$	$1.39^{+0.28}_{-0.18}$	$2.48^{+3.92}_{-0.97}$	$1.59^{+0.37}_{-0.38}$	$1.21^{+0.43}_{-0.33}$	$1.42^{+0.01}_{-0.02}$
HD 219134		2.0	0.10 ± 0.01	0.26 ± 0.03	-	$0.63^{+0.37}_{-0.11}$	$0.16^{+0.05}_{-0.04}$	-	$18.07^{+0.40}_{-0.89}$
GJ 9827	A	9.2	$1.36^{+0.80}_{-0.69}$	$0.25^{+0.05}_{-0.13}$	-	$0.20^{+0.18}_{-0.11}$	$0.25^{+0.08}_{-0.07}$	-	$0.68^{+0.13}_{-0.12}$
	B	9.2	$0.25^{+0.03}_{-0.02}$	-	-	$0.41^{+0.09}_{-0.08}$	-	-	$0.65^{+0.10}_{-0.15}$
	C	9.2	$0.31^{+0.08}_{-0.05}$	-	-	$0.25^{+0.08}_{-0.07}$	-	-	$0.43^{+0.15}_{-0.09}$
Host M									
K2-25		13.9	0.26 ± 0.02	$1.14^{+0.11}_{-0.09}$	-	$6.28^{+0.63}_{-0.62}$	$5.47^{+1.00}_{-0.77}$	-	$8.61^{+0.50}_{-0.45}$
GJ 436	A	3.0	0.11 ± 0.02	$0.31^{+0.07}_{-0.05}$	-	$0.15^{+0.08}_{-0.04}$	$0.051^{+0.018}_{-0.016}$	-	$2.37^{+0.15}_{-0.54}$
	B	3.0	$0.07^{+0.04}_{-0.03}$	$0.75^{+0.15}_{-0.16}$	-	$0.93^{+0.05}_{-0.83}$	0.018 ± 0.005	-	$2.29^{+0.26}_{-1.79}$
	C	3.0	$0.19^{+0.03}_{-0.04}$	$2.12^{+0.70}_{-2.12}$	-	$0.10^{+0.06}_{-0.03}$	$0.050^{+0.081}_{-0.022}$	-	$1.80^{+0.33}_{-0.45}$
	D	3.0	0.23 ± 0.5	$1.21^{+0.17}_{-0.14}$	-	$0.059^{+0.027}_{-0.021}$	$0.054^{+0.016}_{-0.013}$	-	$1.60^{+0.22}_{-0.36}$
	E	3.0	0.24 ± 0.05	$0.93^{+0.26}_{-0.19}$	-	$0.10^{+0.04}_{-0.03}$	$0.025^{+0.015}_{-0.014}$	-	$1.97^{+0.37}_{-0.43}$
	F	3.0	$0.35^{+0.39}_{-0.07}$	-	-	0.11 ± 0.06	-	-	$1.79^{+0.34}_{-0.63}$
	G	3.0	$0.27^{+0.04}_{-0.03}$	-	-	$0.20^{+0.05}_{-0.04}$	-	-	$2.86^{+0.53}_{-0.50}$
	H	3.0	0.12 ± 0.02	$0.53^{+0.08}_{-0.09}$	-	$0.15^{+0.04}_{-0.03}$	$0.055^{+0.012}_{-0.008}$	-	$2.93^{+0.20}_{-0.33}$
LHS 1140		4.6	0.15 ± 0.03	$1.14^{+0.50}_{-0.24}$	-	$0.068^{+0.031}_{-0.016}$	$0.18^{+0.02}_{-0.01}$	-	$0.50^{+0.07}_{-0.08}$
AU Mic	A	3.0	$2.60^{+0.09}_{-0.07}$	$0.916^{+0.003}_{-0.004}$	0.240 ± 0.001	$38.01^{+0.59}_{-0.37}$	$38.37^{+0.50}_{-0.34}$	$71.69^{+0.22}_{-0.35}$	2209 ± 4
	B	3.0	$3.17^{+0.05}_{-0.04}$	$0.963^{+0.002}_{-0.001}$	$0.238^{+0.005}_{-0.004}$	$45.43^{+0.22}_{-0.23}$	$77.27^{+0.34}_{-0.45}$	76.24 ± 0.34	2717^{+5}_{-2}
	C	3.0	$3.19^{+0.04}_{-0.06}$	$0.966^{+0.001}_{-0.002}$	0.239 ± 0.001	$67.25^{+0.50}_{-0.33}$	$44.99^{+0.16}_{-0.24}$	$76.62^{+0.32}_{-0.20}$	2617^{+2}_{-3}
	D	3.0	3.17 ± 0.06	0.953 ± 0.002	0.236 ± 0.001	54.92 ± 0.34	39.83 ± 0.23	72.00 ± 0.23	2351^{+1}_{-3}
	E	3.0	$3.18^{+0.06}_{-0.07}$	0.974 ± 0.003	0.237 ± 0.001	97.58 ± 0.68	$54.36^{+0.34}_{-0.45}$	83.99 ± 0.34	3164^{+4}_{-5}
GJ 3470		9.1	0.28 ± 0.02	$1.45^{+0.60}_{-0.30}$	-	$1.71^{+0.16}_{-0.15}$	$0.62^{+0.26}_{-0.19}$	-	$3.68^{+0.31}_{-0.25}$
GJ 1214	A	4.5	$1.71^{+0.86}_{-0.35}$	$0.25^{+0.06}_{-0.05}$	-	$0.25^{+0.16}_{-0.11}$	0.20 ± 0.07	-	$0.62^{+0.27}_{-0.06}$
	B	4.5	0.30	-	-	0.05	-	-	<0.32

Table 4. Best-fit X-ray spectral models; Hydrogen column density (1); best fit model temperature (2, 3 and 4); best fit emission measure (5,6 and 7) (10^{50} cm^{-3}); unabsorbed flux at Earth, in $10^{-14} \text{ erg s}^{-1} \text{ cm}^{-2}$ (8).